

# Analysis of LGADs for the High Granularity Timing Detector

Susanne Auwens

*Supervisor:* Mengqing Wu

November 9, 2023

## Abstract

For the High Luminosity upgrade of the Large Hadron Collider (LHC) a High Granularity Timing Detector (HGTD) will be installed inside the ATLAS detector. The HGTD will consist of Low Gain Avalanche Detectors (LGAD). Different makes of LGAD were analysed during this study. This study consists of two different parts. The first part is the IV and CV analysis of unirradiated HPK-P2 sensors with different boron concentrations in the gain layer. No irregularities were found here. The second part contains the test beam analysis from the DESY testbeam campaign in 2022. The collected charge and time resolution are studied for three sensors at a fluence of  $1.5 \cdot 10^{-15} \text{ n}_{\text{eq}}/\text{cm}^2$  and  $2.5 \cdot 10^{-15} \text{ n}_{\text{eq}}/\text{cm}^2$ . The data selection was done using a pulse-height cut, geometrical cut, and timing cut. For the charge collection all samples could reach the required charge of 4fC. For the time resolution all samples were able to get below the required 70ps. There were some extra time peaks found for the unirradiated FBK-W19 sensor and for the FBK-W19 sensor with a fluence of  $2.5 \cdot 10^{-15} \text{ n}_{\text{eq}}/\text{cm}^2$ , both are  $2 \times 2$  sensors with one active pad and the other three pads connected to the ground. The extra time peaks for the unirradiated sensor seems to be caused by ringing of electronics. The irradiated sensor had pulses that looked much more like actual signals. For both sensors further investigation is required.

# Contents

<b>1</b>	<b>Introduction</b>	<b>3</b>
<b>2</b>	<b>Background/theory</b>	<b>4</b>
2.1	LGAD . . . . .	4
2.1.1	Semiconductors . . . . .	4
2.1.2	LGAD . . . . .	6
2.1.3	Radiation Damage . . . . .	9
2.2	IV/CV measurements . . . . .	10
2.2.1	IV measurements . . . . .	10
2.2.2	CV measurements . . . . .	10
<b>3</b>	<b>IV &amp; CV measurements</b>	<b>13</b>
3.1	Set-Up . . . . .	13
3.1.1	IV . . . . .	14
3.1.2	CV . . . . .	16
3.2	Methods . . . . .	17
3.3	Results . . . . .	18
3.4	Problems with CV measurements . . . . .	22
3.5	Problems with IV measurements . . . . .	23
<b>4</b>	<b>Testbeam</b>	<b>24</b>
4.1	Testbeam set-up . . . . .	24
4.1.1	Beam telescope . . . . .	26
4.1.2	Data acquisition . . . . .	27
4.1.3	Sensors . . . . .	28
4.2	Data-analysis: Charge collection . . . . .	28
4.2.1	Pulse-height cut . . . . .	29
4.2.2	Geometrical cut . . . . .	31
4.2.3	Time cut . . . . .	32
4.2.4	The effect of the cuts . . . . .	33
4.2.5	Results . . . . .	36
4.3	Data analysis: Time Resolution . . . . .	37
4.3.1	Results . . . . .	38
4.4	Extra time peaks . . . . .	38
<b>5</b>	<b>Conclusion</b>	<b>43</b>
5.1	IV/CV . . . . .	43
5.2	Testbeam . . . . .	46

# 1 Introduction

The Large Hadron Collider (LHC) has played a huge role in the discovery of standard model particles such as the Higgs boson discovery in 2012. To increase the potential of new discoveries the luminosity of the LHC will be cranked up from  $2.1 \times 10^{24} \text{cm}^{-2} \text{s}^{-1}$  to  $7.5 \times 10^{24} \text{cm}^{-2} \text{s}^{-1}$ . The High Luminosity upgrade of the LHC will allow to do further research into the standard model, study properties of the Higgs boson, and search for beyond the Standard Model physics.

One of the main challenges that comes with the HL-LHC upgrade is an increase in pile-up. Pile-up occurs when multiple collisions happen at the same time. With the HL-LHC the pileup multiplicity will increase from an average of 50 to 200 pp collisions per bunch crossing. This will make it more difficult to distinguish between particles originating from high-energy pp collisions - which contain interesting physics but are quite rare - and particles produced by additional low-energy collisions.

In order to mitigate pile-up in the ATLAS experiment, a High Granularity Timing Detector (HGTD) will be installed in the forward region of the ATLAS experiment 1. The HGTD will provide high-precision timing information, allowing to distinguish collisions that occur close in space but are well-separated in time. Therefore, the detector requires to have an average time resolution of 50 ps at the beginning of its operation and 70 ps at the end, at an expected maximum fluence of  $2.5 \cdot 10^{15} \text{n}_{\text{eq}}/\text{cm}^2$ . Other requirements are a hit efficiency of 97% at the beginning and 95% at the end of its lifetime, and a collected charge of over 4fC.

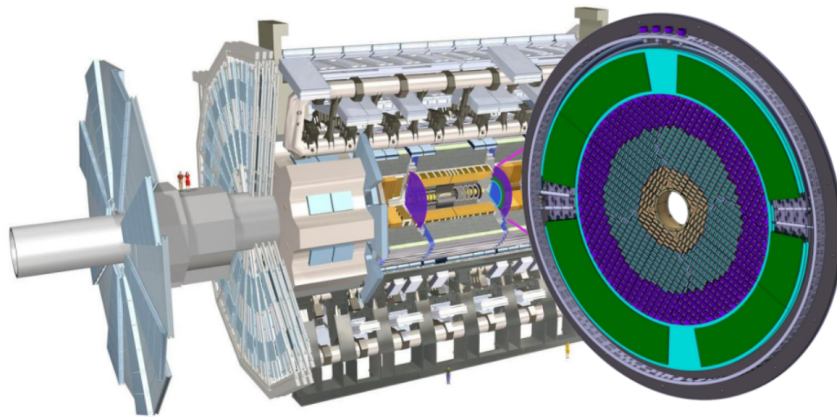


*Figure 1: This figure shows the HGTD and the position with the ATLAS Detector.*

Low Gain Avalanche Detector (LGAD) sensors will be used in order to reach all these requirements. This is a special type of silicon detector that is very thin (in this case  $50 \mu\text{m}$ ) and has an extra gain layer implanted. It provides a moderate gain and is characterised by low noise,

low leakage current, large signals, and good temporal resolution [1].

For this project I studied the behaviour and performance of several different LGAD sensors in order to determine which sensor design is most suitable to be used in the HGTD. I performed I-V and C-V measurements in the lab to study the electrical characteristics of the sensors. I also took part in a testbeam campaign at DESY to study the actual performance of the chip. During the testbeam campaign several sensors with different doses of radiation were tested to see the effect of radiation on the performance. After the testbeam campaign I analysed the testbeam data where I specifically looked into the charge collection and time resolution.

## 2 Background/theory

### 2.1 LGAD

#### 2.1.1 Semiconductors

An LGAD is a specific type of semiconductor detector. The most basic type of semiconductor detector is the PN diode. This is made by taking a base material, often silicon, and applying n and p-doping to the material. An example is seen in figure 2. The p-region contains holes, while the n-region contains electrons. The difference in carrier types creates a diffusion current  $I_{\text{diff}}$  which causes the holes to move to the n-region and the electrons to move to the p-region which results in electron-hole recombination. This leaves a depletion region (or space-charge region) in the middle with no free carriers. What remains in the middle are the ionised atoms with a negatively charged p-region and a positively charged n-region with an intrinsic electric field. The electric field results in a drift current  $I_{\text{drift}}$  in the opposite direction of  $I_{\text{diff}}$ . In the case of no external voltages  $I_{\text{drift}}$  and  $I_{\text{diff}}$  are in equilibrium.

When a particle traverses the detector it deposits energy and creates e-h pairs. In the undepleted regions these e-h pairs recombine quickly and will most likely not reach the electrodes. In the depleted region there is a much smaller chance of recombination and the e-h pairs will drift towards the electrodes under the influence of the electric field. Thus traversing particles can be detected by a spike in the current or a change in voltage over the sensor.

The depletion zone of the detector is also called the active region since this is the part where particles can be detected. When a particle traverses the detector it interacts with the detector material mainly through electromagnetic processes and creates electron-hole pairs (e-h pairs). If the e-h pairs are created in the undepleted region they will recombine before reaching the electrodes. If an e-h pair is created in the depleted region there is a much smaller chance of recombination and the electron and hole will drift towards the electrodes under influence of the electric field. This movement creates a spike in the current and can also be

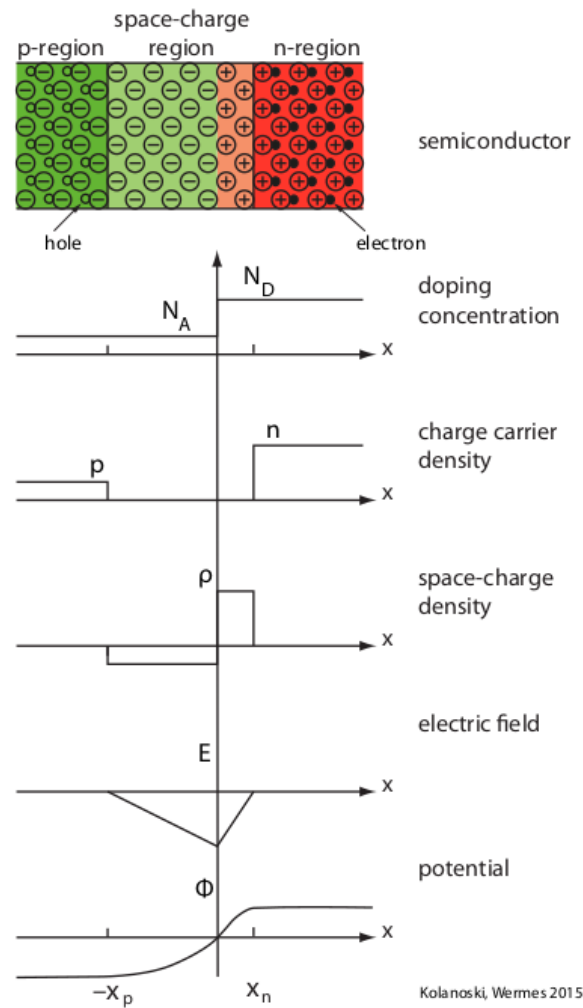


Figure 2: This figure shows an example of a PN-diode. It shows that the doping concentration of the acceptor  $N_A$  and the donor  $N_D$  meet each other in the middle. This creates a depletion region in the middle, hence there is no charge carrier density. This leaves the charged atoms in the middle, resulting in a space charge density. This in turn creates the electric field  $E$  and the potential  $\Phi$ . [2]

measured as a change in voltage.

The active region needs to be maximised in order to increase the efficiency of the detector. This can be done by applying an external bias voltage  $V_{\text{ext}}$ . The depletion region decreases with a forward bias voltages and increases with a reverse bias voltage (see figure 3). In order to create a reverse bias voltage you need to apply a negative voltage to the p-region or a positive voltage to the n-region. This will increase the electrostatic potential, counteract the diffusion current and widen the depletion zone. At a high enough reverse bias voltage the depletion will reach its maximum depth, this is known as full depletion.

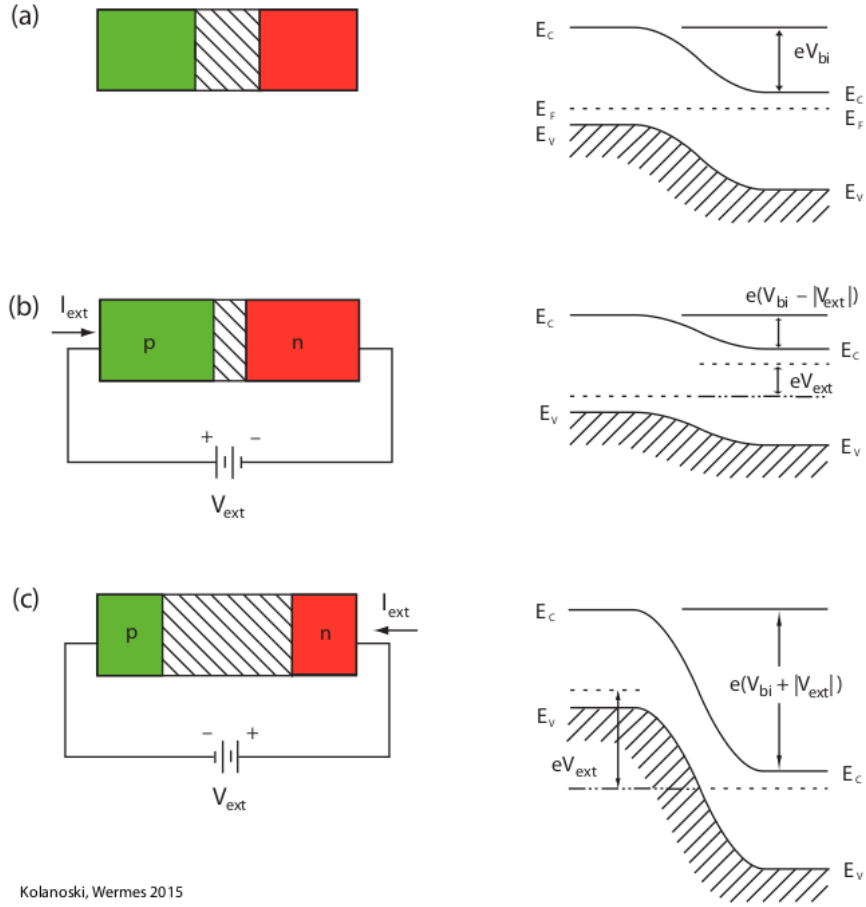


Figure 3: This figure shows a diode with different  $V_{ext}$ : (a) shows the equilibrium situation without  $V_{ext}$ , (b) shows the condition with forward bias, (c) shows the situation with reverse bias voltage applied. [2]

### 2.1.2 LGAD

A typical LGAD is designed as shown in figure 4. It has a  $p^+$ -type implant underneath an  $n^+$  electrode. The  $p^+n^{++}$  junction creates a very high electric field that causes amplification with a typical gain between 10 and 50 [2]. The gain is kept beneath 50 in order to avoid excess amplification noise.

The most important feature of the LGAD is the small time resolution. The time resolution consist of a couple of contributing factors, given by [1] [2]:

$$\sigma_t^2 = \sigma_{\text{time walk}}^2 + \sigma_{\text{noise jitter}}^2 + \sigma_{\text{arrival time}}^2 + \sigma_{\text{distortion}}^2 + \sigma_{\text{TDC}}^2 \quad (1)$$

The time walk component is the result of variations in signal amplitude. If we keep a fixed threshold, like shown in figure 5, we see that a lower amplitude results in a later timestamp. This problem can be reduced by using the constant fraction denominator (CFD) instead.

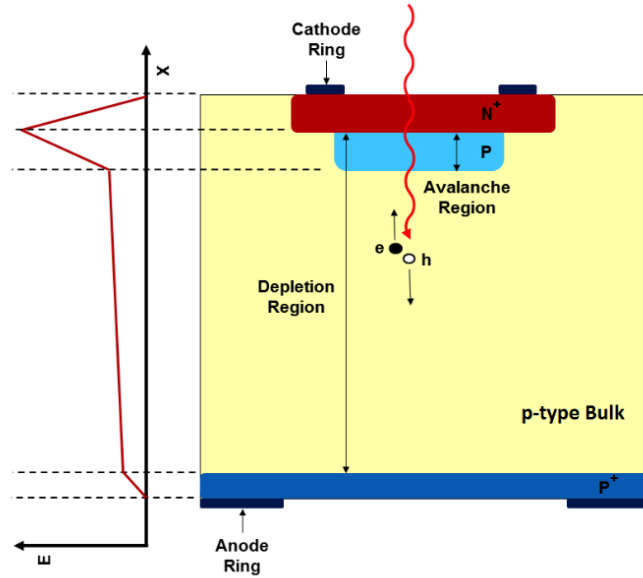


Figure 4: This figure gives a schematic overview of an LGAD. It consists of a p-type bulk, a  $p^{++}$ -type electrode, a  $n^{++}$ -type electrode and a  $p^{+}$ -type implant. The  $p^{+}n^{++}$  junction will create a high electric field resulting in an avalanche region. [3]

The CFD puts the timestamp at a certain fraction of the signal amplitude instead of at a fixed signal height. This will decrease the variation of the timestamps.

The noise jitter term is due to the presence of electronic noise in the signal. As shown in figure 6, the noise can shift the timestamp to an earlier or later time. This jitter can be reduced by increasing the slope of the signal which can be reached by choosing a thinner sensor. However, the sensor can not be too thin since the jitter also depends on the capacitance, and a thinner sensor results in a higher capacitance.

The third component that contributes to the time resolution is the arrival time. Non-uniform charge dispositions along the particle track create irregularities in the signal shape which results in a jitter in the arrival time. A thinner sensor reduces this effect.

The fourth component is the distortion factor. This is due to non-uniform weighting fields and variations in drift velocities. The weighting field determines the induced charge on the read-out electrode depending on the position of the charge. A non-uniform weighting field means that the size of the induced signal depends on the hit position of the particle, resulting in irregular signal shapes. A large homogeneous weighting field can be realised if the electrode is almost the same size as the pitch. A variation in drift velocity also causes variations in the signal shape depending on the location of the particle impact. This can be reduced by increasing the bias voltage to make sure that the electrons reach their maximum drift velocity. The holes however do not reach a final velocity, and so an even higher bias voltage does

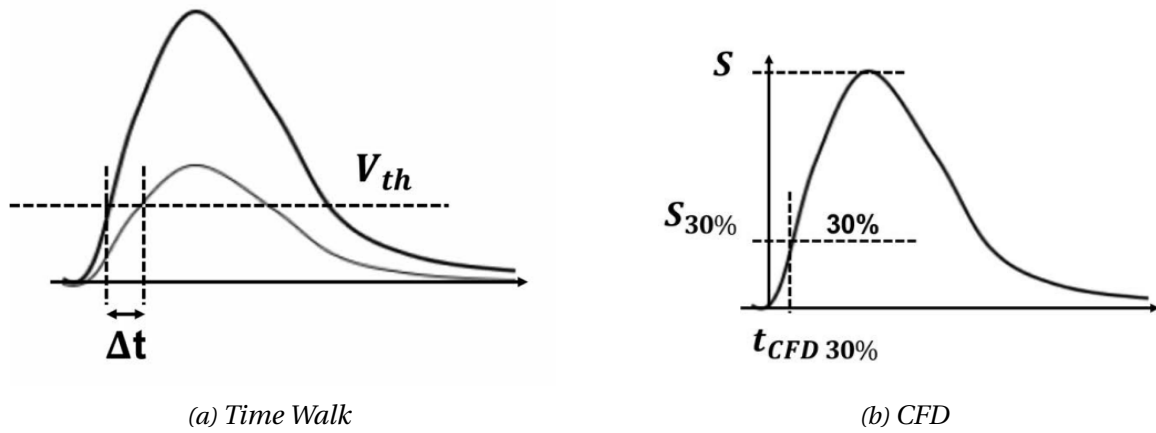


Figure 5: (a) shows the time walk principle. A low-amplitude signal will have a later time stamp than a high-amplitude signal for a fixed threshold. (b) shows how the constant fraction denominator (CFD) works. Here the timestamp is taken at a fraction of 30% of the amplitude. [1]

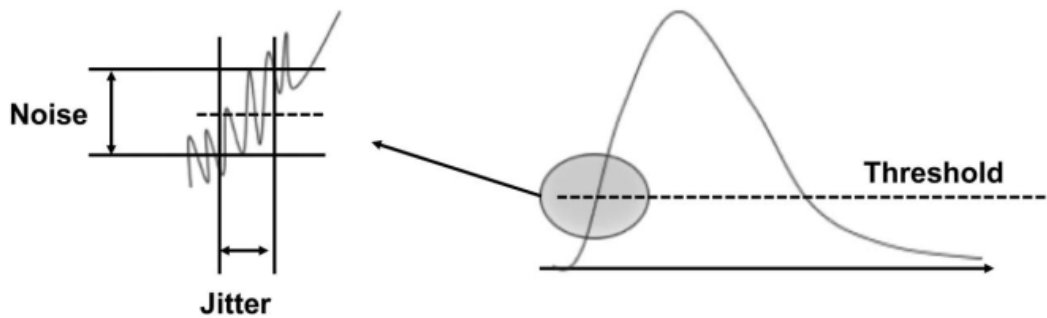


Figure 6: This figure shows how time jitter works: The threshold for the timestamp can be reached later or earlier due to the noise. This causes an insecurity in the timestamp. [1]

result in a sharper signal.

The last component is caused by the Time-to-Digital Converter (TDC). Due to the finite size of TDC bins there is an uncertainty in the time digitisation. However, this term can be made negligible by choosing a GHz TDC.

Taking all these factors in account we come to a specific design for LGAD sensors. They are typically thin (around  $50\ \mu\text{m}$ ), have a pitch in the order of mm, and are operated at a high bias voltage. The amplification implant has a moderate gain between 10 and 50 ensuring a fast rise time of the signal.



### 2.1.3 Radiation Damage

Radiation damage is a very challenging aspect for the LGAD sensor. The sensor will be used inside the ATLAS detector close to the collision point where the sensor is expected to receive a radiation dose of up to  $2.5 \cdot 10^{15} \text{ n}_{\text{eq}}/\text{cm}^2$ . The radiation creates defects in the sensor structure, but mainly the  $\text{p}^+$  type implant is very sensitive to radiation damage. This damage causes a couple of problems that can affect the performance of the sensor. [1] [2]

The first problem is an increase in leakage current. Defects close to the band-gap can create e-h pairs and so the current will increase. The LGAD is extra sensitive to this increase in leakage current because the current will be multiplied by the gain. This causes two types of problems: The first is an increase in power consumption. The second is an increase in shot noise. Shot noise is caused by electron flow over junctions that generate a fluctuation in the current. Shot noise is generally lower than the electronic noise but if it gets too large it will make the sensor more noisy. These problems can be reduced by using a thin sensor, cooling ( $T \approx -30^\circ\text{C}$ ), and using low gain levels. Under these circumstances the shot noise will generally stay below the electronic noise.

The second problem is caused by charge trapping. Charge carriers get trapped in deep radiation defects and this affects the charge collection efficiency. The probability of charge trapping increases with fluence and drift time. For a  $50\text{ }\mu\text{m}$  sensor with an irradiation level in the order of  $10^{15} \text{ n}_{\text{eq}}/\text{cm}^2$  the trapping time is around three times the drift time, thus keeping the chance of trapping low. A simulation [1] shows that it slightly affects the height of the signal, but it does not affect the rise time. This means that the signal is still very much usable.

The third problem occurs due to a variation in doping concentration caused by acceptor removal and creation. This is a problem especially for the gain implant since the gain is one of the most important features of the LGAD. Acceptor removal is still not completely understood, but one of the suggested mechanisms is a sort of kick-out mechanism. Silicon gets displaced outside of the lattice and interacts with the doping atom (Boron), which inactivates the Boron. There are two proposed methods for increasing radiation hardness. The first one is to substitute Boron for Gallium. Gallium is heavier and the inactivation rate should be lower. A second option that is being studied is adding additional Carbon atoms. This should replace the Boron in ion-defects.

The inactivation of Boron in the gain layer leads to a reduction in gain due to a lower electric field. This process can be compensated by increasing the bias voltage. However, if the bias voltage gets high enough (500-750V for  $50\text{ }\mu\text{m}$  thickness) there will be a multiplication process in the bulk as well. This will rapidly lead to a breakdown situation.

## 2.2 IV/CV measurements

Current-voltage measurements (IV) and capacitance-voltage measurements (CV) are used for the static characterisation of the sensor. The leakage current and capacitance will be measured in absence of external particles. These measurements are used to determine the gain-layer voltage ( $V_{gl}$ ), the full-depletion voltage  $V_{vd}$ , and the leakage current  $I_{leak}$  at the level of  $V_{vd}$ .

### 2.2.1 IV measurements

For the IV measurements the leakage current gets measured for increasing bias voltages. In case of the LGAD this will be reverse bias voltage with negative voltage to the back in order to increase the depletion regions. Leakage currents consists of surface and volume contributions. The bulk contributions are mainly from thermal generation of e-h pairs in the depleted regions. This often happens in impurities inside the lattice and therefore we see a much higher leakage current for irradiated sensors. The current that gets generated this way depends on the size of the depleted region and on the temperature.

An example of such an IV-measurement is shown in figure 7. This figure compares the IV curve of a PIN diode with the IV curve of an LGAD (in this picture called UFDS, Ultra Fast Silicon Detector). Characteristic for the LGAD is the jump in leakage current around 25V. This jump is caused by the gain layer becoming active and the size of the jump depends on the gain. The other point of interest is the exponential increase in the end. This is the breakdown of the sensor. This happens for the PIN diode as well but is not displayed in this picture. Breakdown happens when the electric field in the bulk gets high enough to start multiplication just like in the gain layer.

### 2.2.2 CV measurements

Since the LGAD has a depletion region with no charge carriers we can model it as a parallel plate capacitor with the depletion zone being the dielectric. Therefore we can use the following formula for the capacitance:

$$C = \epsilon_0 \epsilon_{Si} \frac{A}{d} \quad (2)$$

In this formula  $A$  is the area,  $d$  is the thickness of the depletion zone,  $\epsilon_0$  is the permittivity of free space, and  $\epsilon_{Si} \approx 11.9$  is the permittivity of the silicon. This can be used to estimate the maximum capacitance that will be measured.

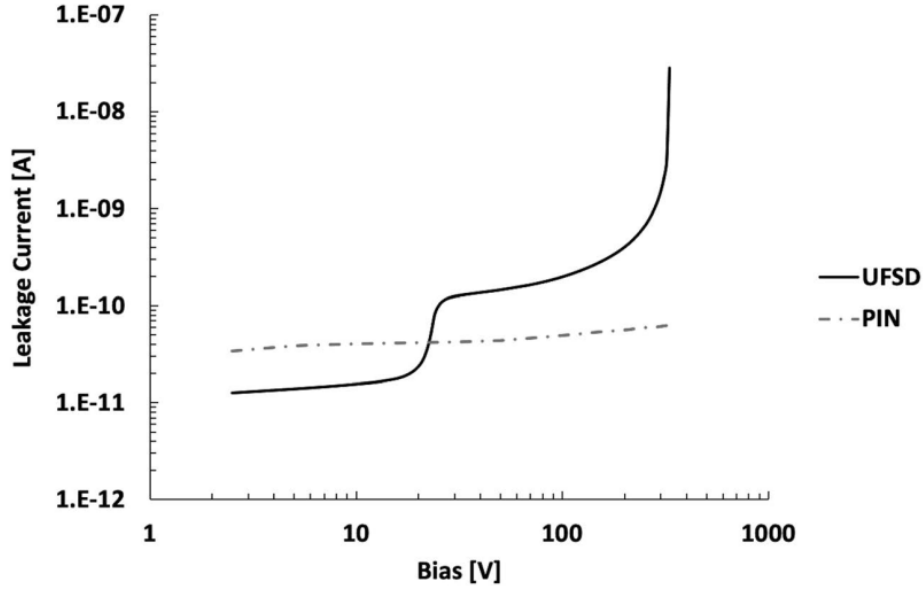


Figure 7: This figure shows the IV-curve for an LGAD (UFSD in this picture) in solid black and the IV-curve of a PIN-diode in a grey dotted line. [1]

The CV measurement itself is actually an impedance measurement [1] [4]. For the measurement we apply a DC bias voltage and an AC voltage with constant frequency and amplitude to the sensor. Then an AC impedance meter can measure the amplitude and phase angle of the impedance and those can be converted to rectangular forms with an in-phase vector and an imaginary out of phase vector. This results in two models as shown in figure 8. On the left is the parallel model with conductance  $G_p$  (or resistance  $R_p = 1/G_p$ ) and capacitance  $C_p$ , on the right is the series model with resistance  $R_s$  and capacitance  $C_s$ . Formulas for both models are given below:

$$Z = R_s - j \frac{1}{\omega C_s} = \frac{1}{Y} \quad (3)$$

$$Y = G_p + j\omega C_p \quad (4)$$

The formula for the impedance  $Z$  is used for the series model and the formula for the admittance  $Y$  ( $Y = 1/Z$ ) is used for the parallel model. For both methods we need to take the imaginary part and adjust for  $\omega = 2\pi f$  where  $f$  is the frequency of the AC signal. For unirradiated sensors both methods can be used since the leakage currents are low and the capacitance terms are dominant. For unirradiated sensors with high leakage currents only the parallel model can be used. That is because the series model does not allow for a leakage current.

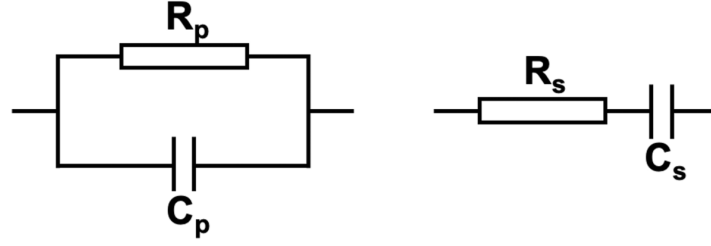


Figure 8: This figure shows the two different models for the CV measurement. It has the parallel model on the left with resistance  $R_p$  and capacitance  $C_p$ , and it has the series model on the right with resistance  $R_s$  and capacitance  $C_s$  [1]

To check the accuracy of the measurements one can use the dissipation factor:

$$D = \frac{G_p}{\omega C_p} \quad (5)$$

This calculates the ratio between the real vector  $G_p$  and the imaginary vector  $C_p$ . For an accurate measurement we need a small dissipation factor.

The results of these measurements will look like the CV-curve shown in figure 9. This figure compares the CV-curve of the LGAD (UFSD in the picture) and that of a PIN. We first look at the full depletion voltage  $V_{vd}$  which is at the point where the graph becomes horizontal. We can understand this by looking at formula 2. Here we see that the capacitance depends on the depletion depth  $d$ , so if the full depletion depth is reached that means that the capacitance is at its lowest and becomes constant. The other point of interest here is the sudden drop, this happens when the full depletion depth of the gain layer  $V_{gl}$  is reached.  $V_{gl}$  depends on the boron dose  $N_A$  and the depth  $d$  and width  $w$  of the multiplication layer as:

$$V_{gl} \propto \left(1 + 2 \frac{d}{w}\right) N_A w^2 \quad (6)$$

This means that for sensors with the same gain layer width and depth,  $V_{gl}$  depends entirely on the gain layer dose.

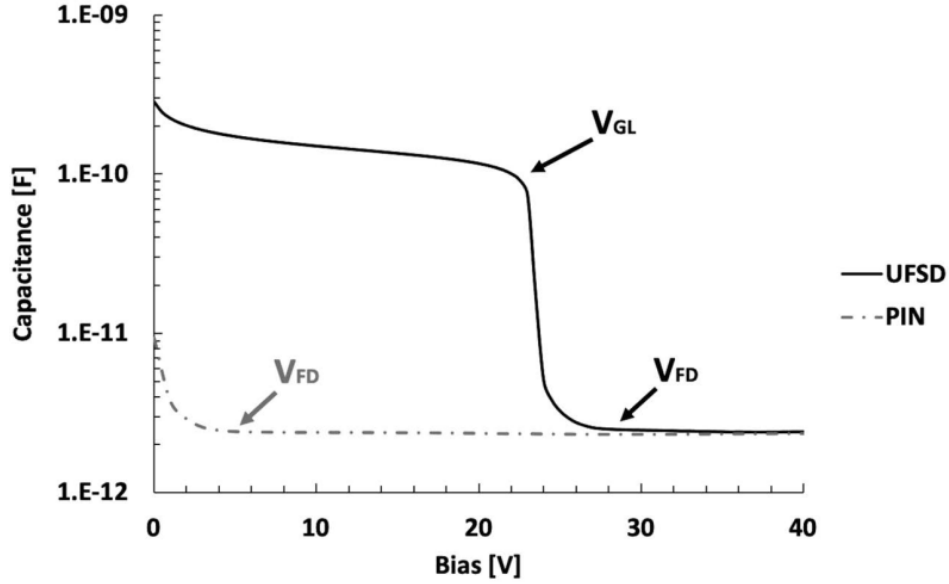


Figure 9: This figure shows the CV-curve of an LGAD (here called UFSD) in the solid black line and the CV-curve of a PIN-diode with the dashed grey line. [1]

### 3 IV & CV measurements

#### 3.1 Set-Up

The IV and CV measurements were performed with a set of HPK-3.2 sensors, made by Hamamatsu. These sensors are used to compare the IV and CV measurements between the different sites. The properties of the HPK samples are given in table 1 [3]. The set contained eight samples from eight different wafers which are displayed in table 2. There are four  $1 \times 1$  samples and four  $2 \times 2$  samples of which the  $2 \times 2$  samples have under bump material (UBM). Wafers that are displayed in the same row have the same boron dose for the gain layer, so wafer 28 and wafer 25 are the same in terms of gain layer. The top row has the highest boron dose, the bottom row has the lowest boron dose, and for the two middle rows the boron dose should be evenly spaced between the highest and lowest dose.

Table 1: Properties of the samples used for IV and CV measurements.

Name	Thickness [ $\mu\text{m}$ ]	Area [ $\text{mm}^2$ ]	Gain layer dopant	Gain layer depth [ $\mu\text{m}$ ]	Gain layer depletion [V]	Full depletion [V]
HPK-3.2	50	$1.3 \times 1.3$	Boron	2.2	55	65

To distinguish between measurement of the different pads of the  $2 \times 2$  sensors, the individual

Table 2: This table shows the wafer numbers of the HPK-3.2 samples for the IV and CV measurements. Wafers in the same row have the same boron dose for the gain layer.

1×1 HPK-P2	2×2 HPK-P2	Boron dose gain layer
W28	W25	Highest
W33	W31	Second highest
W37	W36	Second lowest
W43	W42	Lowest

pads were numbered. This is done as shown in figure 10.



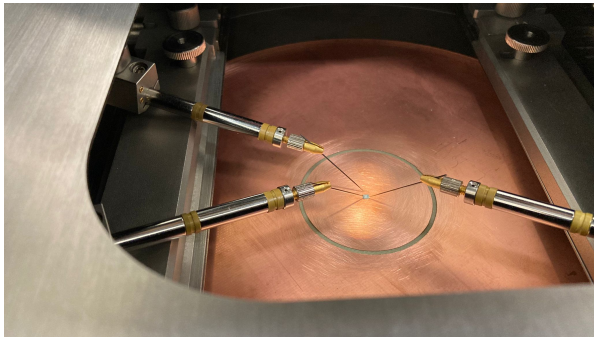
Figure 10: This is a picture of a HPK 2×2-sensor. The pads are numbered 1 to 4 as shown.

### 3.1.1 IV

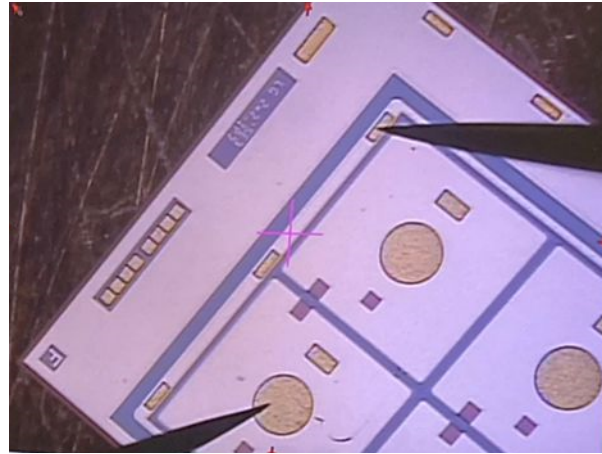
The IV measurements were done on the probestation pictured in figure 11. The sample was connected as shown in figure 12. Three needles were used: Needle 1 is connected to the pad and needle 2 is connected to the guard ring, both are connected to the ground of the source measure unit. Needle 3 is put on the insulated copper plate and is used to apply a negative voltage to the back of the sensor. Normally the negative voltage can be applied from the chuck but the expected currents are so low that it is necessary to insulate the sample from the chuck in order to reduce noise. The needles are connected to the outside of the probestation with the use of coaxial cables and from there connected to the SMU (Keithley 2410 1100V) with banana cables. For the 2×2-samples only one of the pads was connected, the other three were left floating.



(a)



(b)



(c)

Figure 11: (a) Shows the probestation. The needles are set-up left and right and connected to the side of the probestation with coax cables. The sample is placed in the middle. (b) shows how the needles. One is put on the copper plate, one on a pad and one on the guard ring. (c) shows an image from the microscope where one needle is connected to a pad and one connected to the guard ring.

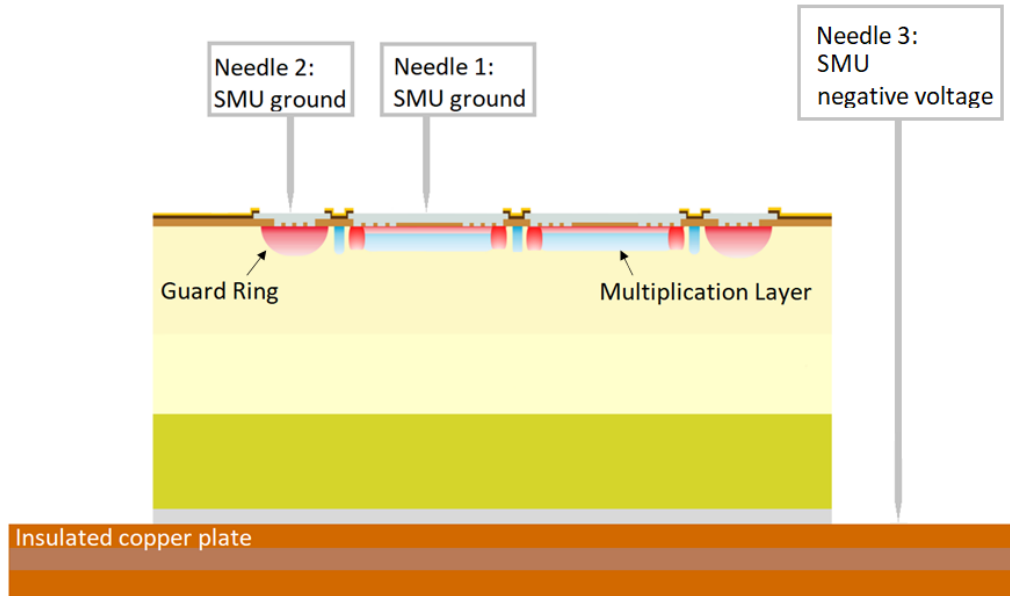


Figure 12: This is a cross section of the  $2 \times 2$  LGAD that shows how the needles were connected for the IV measurements. Needle 1 was placed on the pad and connected to the ground of the SMU. Needle 2 also connected the guard ring to the ground of the SMU. The LGAD was placed on an insulated copper plate to reduce noise from the probestation. The negative bias voltage was applied to the back of the LGAD using needle 3 that connected to the insulated copper plate and the negative voltage of the SMU.

The measurements were done using automatic measurements. The connection was checked before the start of the measurement, this was done by applying a small positive voltage (forward bias) of 0.200V. After that the measurements were started with a compliance current of  $0.5 \mu\text{A}$ , step size of 0.5 V, and a wait time between measurements of 1s.

### 3.1.2 CV

For the CV measurements the probestation needles had to be connected to the CVU (Keithley 4200-SCS). However, since the maximum voltage for the CVU was  $\pm 30\text{V}$  a bias tee was used to be able to reach voltages of up to 200V. The bias tee (4205-RBT) was connected as shown in figure 13 [4]. The high side of the CVU (H CUR and H POT) was connected to the AC input of the bias tee, providing the AC signal. The sense and force of the bias tee were connected to the SMU of the CVU which provides the DC voltage. The AC & DC output of the bias tee were connected to the back of the sample, and the pad of the sample was connected to the low side of the CVU (L POT and L CUR).

The CV measurements were done using the parallel model (see section 2.2.2). The manual stated that measurements had to be done at 10 kHz at room temperature, but this resulted in huge spikes at lower capacitance. Therefore the measurements were done at 1 MHz instead,



which should be fine for unirradiated sensors as discussed in section 2.2.2. The quality of the measurements will be checked with the dissipation factor, see equation 5 at page 12.

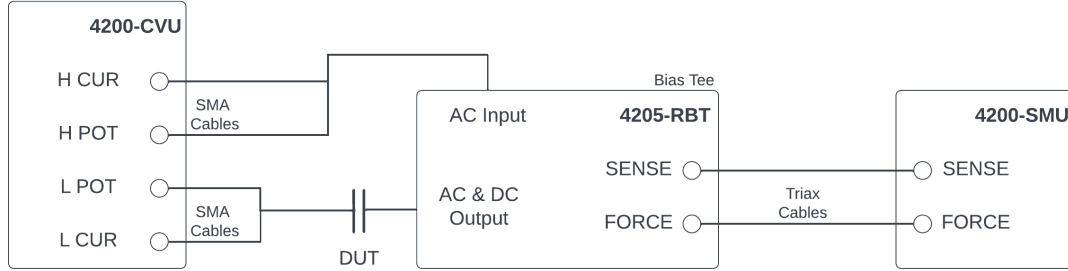


Figure 13: This figure shows how the DUT is connected to the bias tee and CVU. Displayed here are the CVU (4200-CVU), the bias tee (4205-RBT), the external SMU (4200-SMU) and the DUT. The backside of the DUT is connected to the AC & DC output of the bias tee and the pad of the DUT is connected to the low side (L POT and L CUR) of the CVU. [4]

### 3.2 Methods

The IV and CV measurements will be used to determine the depletion voltage of the gain layer  $V_{gl}$ , the full depletion voltage  $V_{vd}$ , and the leakage current  $I_{leak}$  at the voltage level of  $V_{vd}$ .

The method for finding  $V_{vd}$  and  $V_{gl}$  are shown in figure 14. The graphs look a different compared to the examples discussed in section 2.2.2 since the y-axis is different, figure 14 uses  $1/C^2$  instead of  $C$ .  $V_{vd}$  is located at the knee of the graph and is found by fitting two lines as shown in figure 18b.  $V_{gl}$  is at the ankle of the graph and fig 18a shows a zoomed in version of the graph.  $V_{gl}$  is also found by using two linear fits.

After finding  $V_{vd}$  and  $V_{gl}$  we can have a look at the IV-curve to find  $I_{leak}$  at  $V_{vd}$ . An example is shown in figure 15. The shape of this graphs looks a bit different than the graph in section 2.2.1, this is because this figure uses linear scales for both axes instead of logarithmic scales. Because of the spiky behaviour it was difficult to determine  $I_{leak}$ . Therefore a third degree polynomial was fitted using the least squares method, to check this fit we looked into the correlation coefficient  $R^2$ . An  $R^2$  close to 1 indicates a good fit. Finally  $I_{leak}$  was found by taking the current at  $V_{vd}$ .

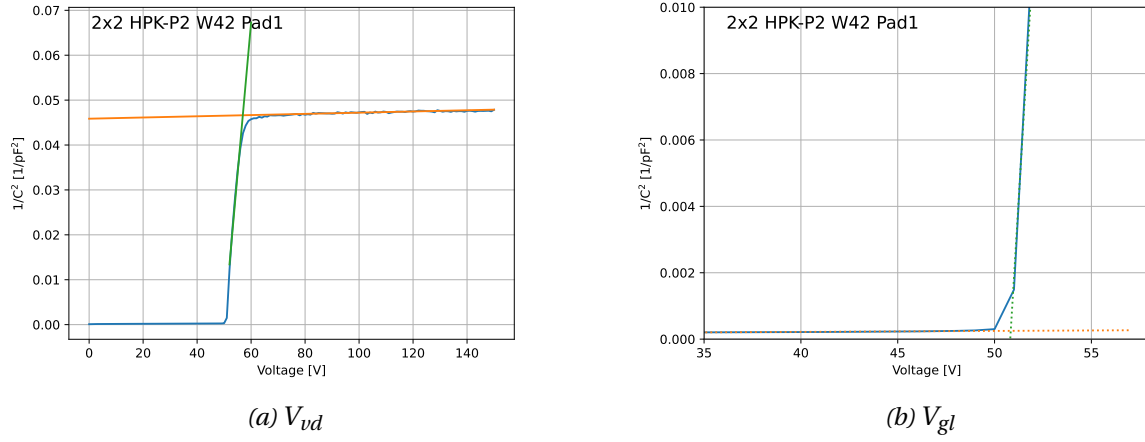


Figure 14: These are CV curves with the bias voltage  $V$  on the x-axis and inverse capacitance squared  $1/C^2$  on the y-axis. This figure shows the method for finding the full depletion voltage  $V_{vd}$  and the gain layer depletion voltage  $V_{gl}$ . (a) shows the method for finding  $V_{vd}$ . The orange and green line are fitted with a linear fit and  $V_{vd}$  is taken as the intersection. (b) is the zoomed in graph and shows the method for finding  $V_{gl}$ . The orange and green line are drawn using a linear fit with  $V_{gl}$  at the intersection.

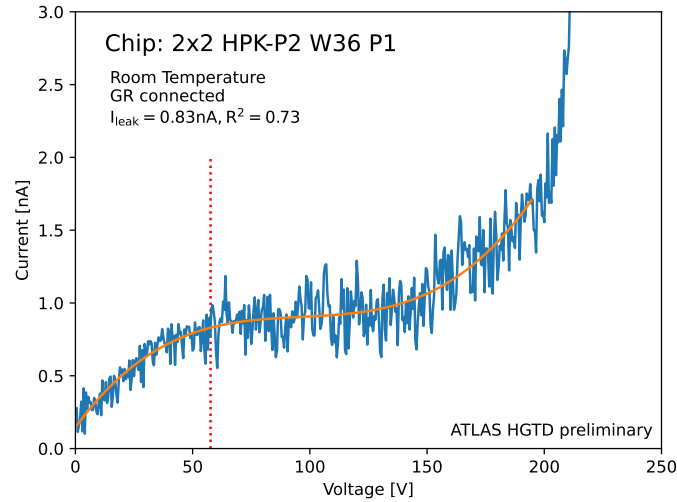


Figure 15: This plot shows the method for finding the leakage current. The red line is the  $V_{vd}$  which was found using the CV plot. The orange line is a third degree polynomial fit. The intersection of the fit with  $V_{vd}$  gives the leakage current  $I_{leak}$ .

### 3.3 Results

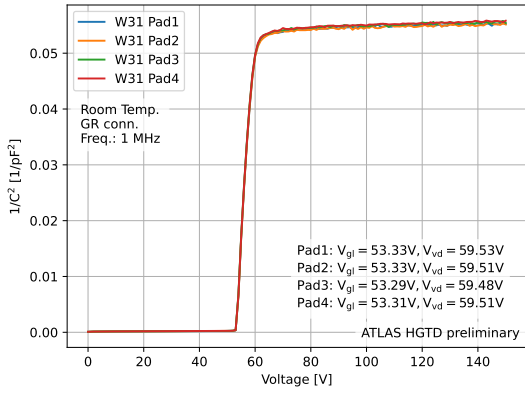
For the results several comparisons between the samples were made. First the homogeneity of the pads of the  $2 \times 2$  samples were checked. All pads within a sample should be the same,

if not this could indicate a defect of one of the pads. Next the  $1 \times 1$  samples were compared, this is to check the behaviour of different boron doses. The same is done for the  $2 \times 2$  samples, but here only one pad of each sample gets chosen. Last the  $1 \times 1$  sample gets compared to the  $2 \times 2$  sample with the same boron dose, this way we can see the effect of the under-bump-metallisation (UBM) that is used in only the  $2 \times 2$  samples.

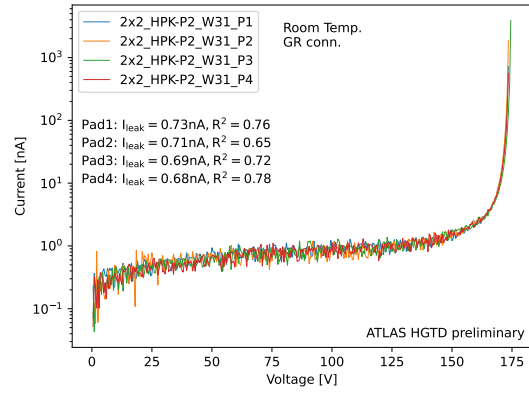
The results for the pad comparisons are shown in figure 16. We see that the pads of wafer 31 all look the same with the same  $V_{gl}$  and  $V_{vd}$ . There is a minor variation in  $I_{leak}$ , but that is expected with the spiky behaviour of the IV curve. The pads for wafer 25 showed the same behaviour. For wafer 36 the  $V_{gl}$  and  $V_{vd}$  are the same for all pads as expected. We do see an increased  $I_{leak}$  for pad 1, which is around 0.2nA higher than the other pads. The increased  $I_{leak}$  could indicate some small defect. We also see a difference in capacitance at high voltages, namely pad 1 and 2 have a lower capacitance than pad 3 and 4. In wafer 42 we see the same issue, here the capacitance for pad 1 and 2 is higher compared to pad 3 and 4. The values for  $V_{gl}$ ,  $V_{vd}$ ,  $I_{leak}$  are the same for all pads of wafer 42. Regarding the issue with the difference in capacitance: Since the issue is located on one side of both sensors and because the capacitance depends on the thickness of the depletion region (see equation 2) this could be caused by applying more pressure to one side of the sample, for instance during the cutting of the wafer. Overall the pads of all the sensors look quite homogeneous apart from the high leakage current for pad 1 of wafer 36 we can safely compare the  $2 \times 2$  sensors by only taking in account one pad of each sample.

The IV-curves and CV-curves that compare doping concentrations are shown in figure 17. The doping concentration, gain layer depth, and gain layer width all influence the  $V_{gl}$  as described in equation 6 on page 12. Since the gain layer depth and gain layer width are the same for all wafers  $V_{gl}$  depends only on the boron concentrations. For the highest boron concentration we expect the highest  $V_{gl}$  and the lowest  $V_{bd}$ . This is exactly what we see for both the  $1 \times 1$  and  $2 \times 2$  wafers. What we do notice for the  $2 \times 2$  wafers is that the  $V_{bd}$  are not equally spaced, but wafer 36 and 42 are very close together. This is likely due to variations in the doping concentration.

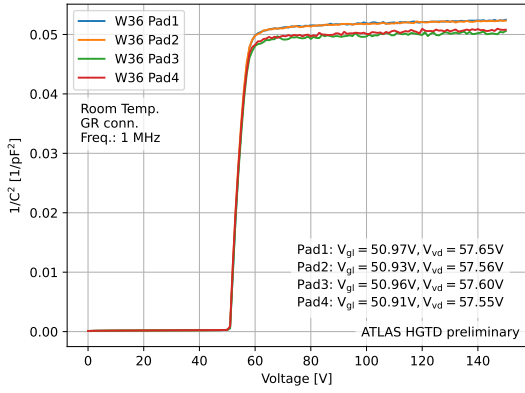
The last comparison is between  $1 \times 1$  and  $2 \times 2$  wafers with the same boron dose. The  $2 \times 2$  samples have UBM material, the  $1 \times 1$  samples do not. According to the technical design report [3] the  $I_{leak}$  should be twice as large for samples with UBM compared to samples without. Figure 18 shows the results of this comparison for wafer 43 and wafer 42.  $V_{gl}$  and  $V_{vd}$  are the same for both sensors which is expected for samples with the same boron dose. The only difference we see is in  $I_{leak}$  which is indeed twice as high for the  $2 \times 2$  sample with UBM.



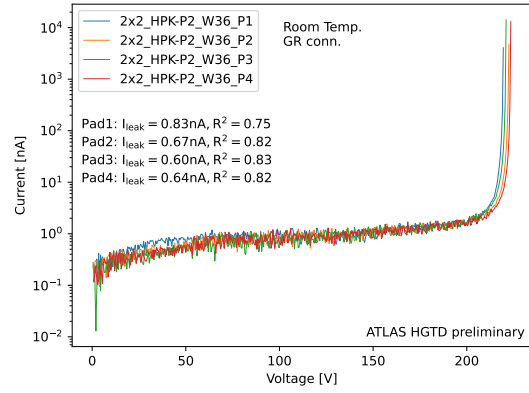
(a) CV Wafer 31



(b) IV Wafer 31

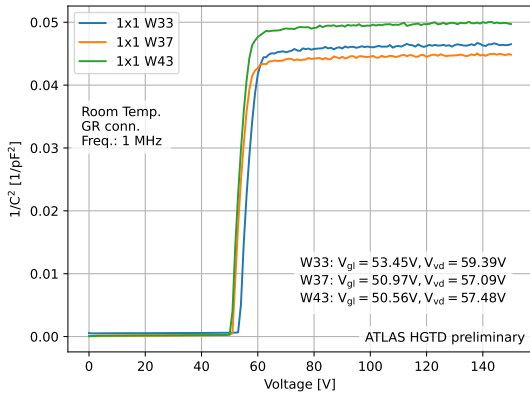


(c) CV Wafer 36

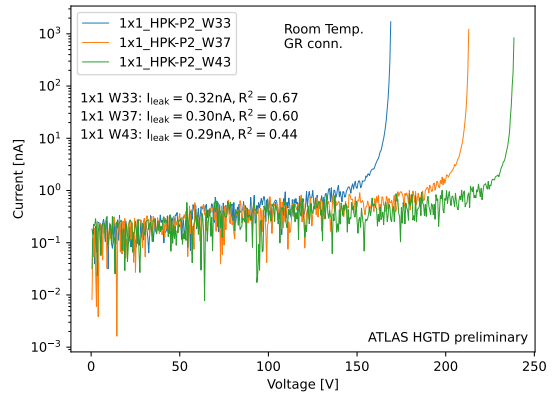


(d) IV Wafer 36

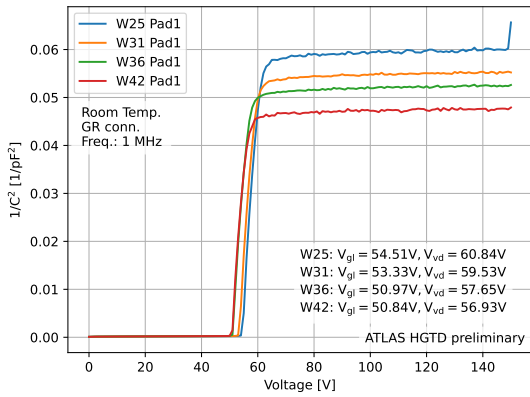
Figure 16: These graphs show the CV and IV curves of pads from the same wafer. (a) Shows the CV curves for the pads of Wafer 31 and (b) shows the corresponding IV curves. (c) and (d) show respectively the CV and IV curves of wafer 36.



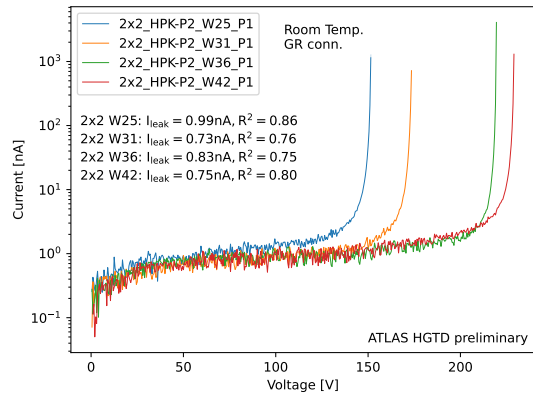
(a) CV of 1x1 wafers.



(b) IV of 1x1 wafers.



(c) CV of 2x2 wafers.



(d) IV of 2x2 wafers.

Figure 17: These graphs compare the CV and IV curves for wafers with different gain layer boron doses. (a) and (b) are the CV and IV curves of the  $1 \times 1$  wafers. (c) and (d) are the CV and IV curves of a single pad of the  $2 \times 2$  wafers.

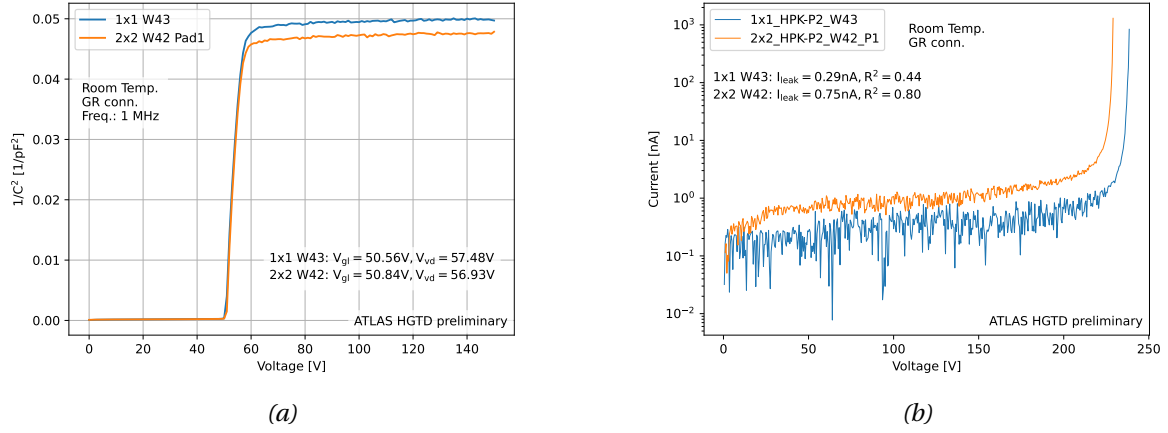


Figure 18: These figures compare the IV and CV curves of a  $1 \times 1$  wafer without UBM with a  $2 \times 2$  wafer with UBM both with the same gain layer boron dose.

### 3.4 Problems with CV measurements

To check if the capacitance is as expected we can compare the CV measurement with the formula for the capacity. We take equation 2 from page 10 with  $\epsilon_{tetsi} \approx 11.9$ , a maximum depletion depth of  $d = 50\mu m$ , and an area of  $A = 1300 \times 1300 \mu m^2$  the expected maximum capacitance will be  $C \approx 3.6pF$ , or  $0.077pF^{-2}$ . We also checked with the measurements in the technical design report, there we see a capacitance of around 4 pF. We see that our measurements are close to these values, but slightly higher. This could mean that the measurements are not entirely accurate, or the depletion depth is not exactly  $50 \mu m$ .

Another thing to look further into is the AC frequency of the measurements. The test procedure document stated that CV measurements done at room temperature should be performed at 10kHz, at least for irradiated sensors. However, the test equipment was at its limit at this frequency and it resulted in a very spiky CV-curve at high voltages as visible in figure 19a. It also shows that the 100kHz and 1MHz measurements are much more stable. However, as shown in figure 19b, we see that the dissipation factor for 1MHz measurements is much higher. This indicates that the measurements done at 1 MHz have a lower accuracy. However, the effect of the frequency on  $V_{vd}$  and  $V_{gl}$  was checked and seemed negligible, results are shown in table 3. This table shows that there is barely a difference between the 1MHz and 100kHz measurements while the  $V_{vd}$  for 10kHz shows a difference of about 0.3V. Although it must be noted here that the 10kHz measurements were much more difficult to fit, since a small change in fit region had a big influence. Because of this difficulty and the seemingly negligible influence it was decided to use the 1MHz measurements.

There are some adjustments that could be done for future measurements in order to improve the measurements. The first important thing is that the cables were rather long and

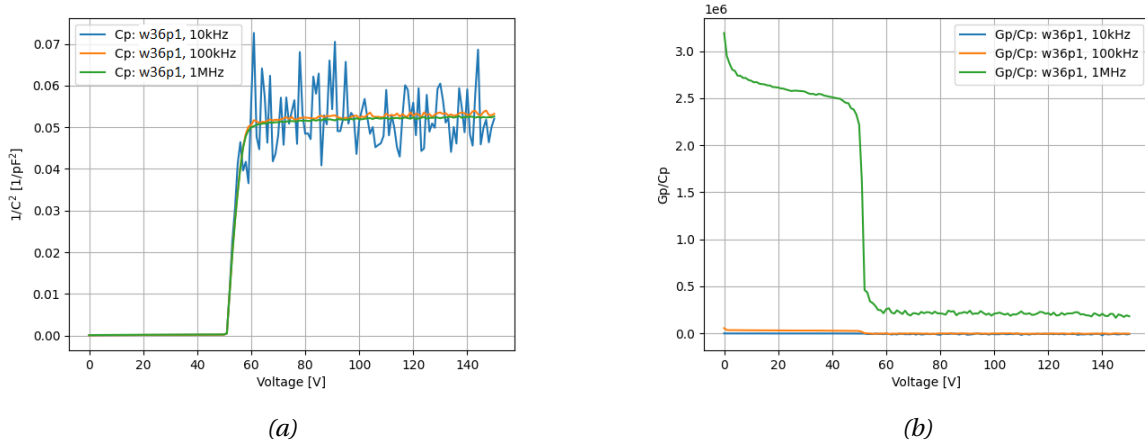


Figure 19: These plots compare CV measurements at an AC frequency of 10kHz, 100kHz and 1MHz of W36 pad 1. (a) shows the CV curves, (b) shows the dissipation factor.

Table 3: This table shows  $V_{vd}$  and  $V_{gl}$  for different AC frequencies. All measured for sample W36 pad 1.

$f$ [kHz]	$V_{vd}$ [V]	$V_{gl}$ [V]
1000	57.01	50.08
100	57.04	50.12
10	56.72	51.53

there was no calibration done for cable length. These calibrations are especially important for high frequency measurements because longer cables will create a longer time delay. For low frequencies this might not be very noticeable, but for higher frequencies the same time delay can create a significant phase shift. Therefore the measurements could likely be improved by calibrating the system. The second thing is that there was no temperature control or measurement. Since the measurements depend on temperature it would be at least good to see if some of the results were influenced by that. Finally, it would be interesting to see what the results would look like if the series model was used instead of the parallel model, since we are dealing with unirradiated samples it should be possible to use the series model.

### 3.5 Problems with IV measurements

Also the IV-curves were dealing with spiky measurements. In figure 18 it looks like the spikes are worse for 1 sensors compared to the  $2 \times 2$  sensors, but this is due to the logarithmic scale. There could be a couple of reasons for the spiky behaviour. The first is bad connection. However, this is unlikely the cause since all sensors were dealing with the issue and reconnecting did not make a difference. A second reason could be the SMU that was used. When the first

sample was measured manually it already became clear that the current did not stabilise. The current measurement accuracy for the SMU is shown in figure 20. For future measurements it would be better to use a SMU that could handle lower ranges.

CURRENT MEASUREMENT ACCURACY (LOCAL OR REMOTE SENSE) Keithley 2410 1100V SourceMeter (SMU)

RANGE	DEFAULT RESOLUTION	VOLTAGE BURDEN <sup>3</sup>	ACCURACY (1 Year) 23°C ±5°C ±(% rdg. + amps)
1.00000 µA	10 pA	>1 mV	0.029% + 300 pA
10.0000 µA	100 pA	>1 mV	0.027% + 700 pA
100.000 µA	1 nA	>1 mV	0.025% + 6 nA

Figure 20: This figure shows the accuracy for current measurements for the Keithley 2410 1100V SourceMeter. The 1.0000µA range was used for the measurements.

Another method for creating a more accurate graph would be to do multiple measurements per bias voltage level and take the average or the mean. Due to time constraints this was done for only one chip and the results are shown in figure 21 and table 4. We see that the spikes are reduced a lot, both for the median and the mean. Theoretically the median should be a better method since this is less sensitive for single outliers, but in this case we see that the median has a slightly higher correlation coefficient for the fit. Although the overall shape of these combined measurements look good, the  $I_{\text{leak}}$  of this series of measurements is lower than the  $I_{\text{leak}}$  of the measurements that were done before, 0.12 – 0.13nA compared to 0.290nA. This could be explained by the construction work that was going on during the repeated measurements. The construction work was taking place close to the lab, this probably caused vibration which result in a bad connection and thus a lower  $I_{\text{leak}}$ .

Table 4: This table shows the leakage current  $I_{\text{leak}}$  and the correlation coefficient  $r^2$  for a single IV measurements, the mean of 10 IV measurements, and the median of 10 IV measurements.

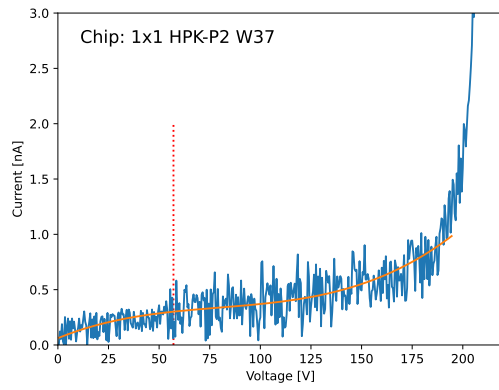
Method	$I_{\text{leak}}$ [nA]	$R^2$
Single	0.123	0.36
Mean of 10	0.131	0.66
Median of 10	0.122	0.57

## 4 Testbeam

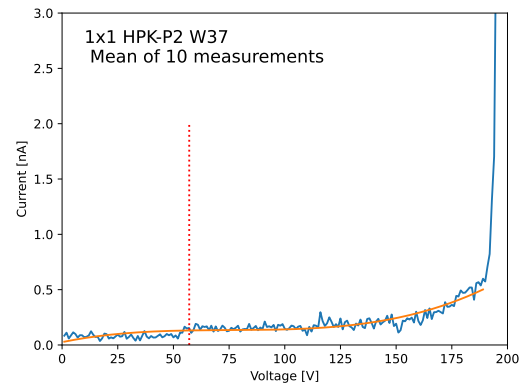
### 4.1 Testbeam set-up

The HGTD testbeam campaigns provide us with timing and position information in order to evaluate sensor efficiency, charge uniformity as a function of the particle incident position, and timing resolution. This study analyses the data from the February 2022 campaign at the

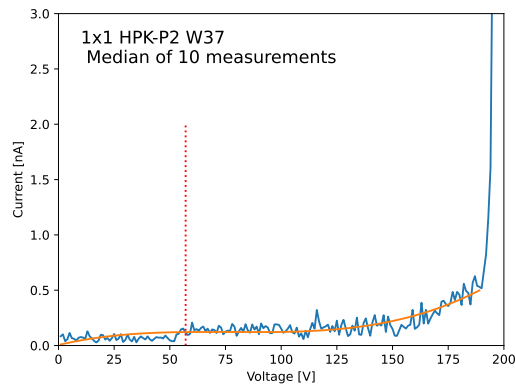




(a) Single measurement



(b) Mean of 10 measurements



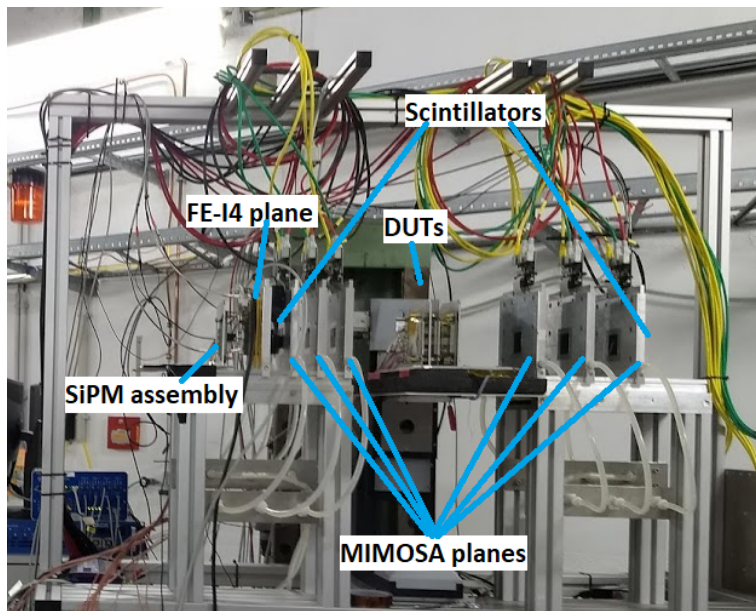
(c) Median of 10 measurements

Figure 21: These are the CV plots for W37 and show the difference between a single measurement, the mean out of 10 measurement, and the median out of 10 measurements.

DESY II testbeam facility [5]. A total of thirteen DUTs (Device under test) were tested with a 5 GeV electron beam.

#### 4.1.1 Beam telescope

The beam telescope used in the DESY testbeam is a EUDET-type telescope [6] and is shown in figure 22. The DUTs are placed in the middle of the telescope with three MIMOSA planes on the left and three on the right. Each MIMOSA plane has an area of  $10,6 \times 21,2\text{mm}^2$  and a pixel size of  $18,5 \times 18,5\mu\text{m}^2$ , and are used to track the position of the particles with a resolution of a few micrometers.



*Figure 22: This is the beam telescope at DESY with the direction of the beam line from right to left. This picture contains the MIMOSA tracking planes with the two DUTs in the middle, scintillators at both ends, and at the end the FE-I4 plane and the SiPM assembly. [7]*

The triggering is done with the FE-I4 plane and the two scintillators (figure 23). The scintillators are placed on both ends of the telescope and connected to a photo multiplier tube. The FE-I4 plane is placed on the end of the telescope and is also used for DUT alignment. The dimensions of the FE-I4 plane are  $16,8 \times 20,0\text{mm}^2$  with a pixel size of  $50 \times 150\mu\text{m}^2$ .

The SiPM (silicon photo multiplier) at the end of the telescope forms the timing reference system together with a quartz bar. The time resolution of  $(63,3 \pm 0,9)$  ps is comparable to the expected time resolution of the DUT, and therefore sufficient for the timing measurements.

The cooling system for the (irradiated) DUTs consists of a Styrofoam box with a separate compartment for dry ice. The temperature was monitored and ranged between -40 to -25

°C. The box also provided a light tight environment for the DUTs.

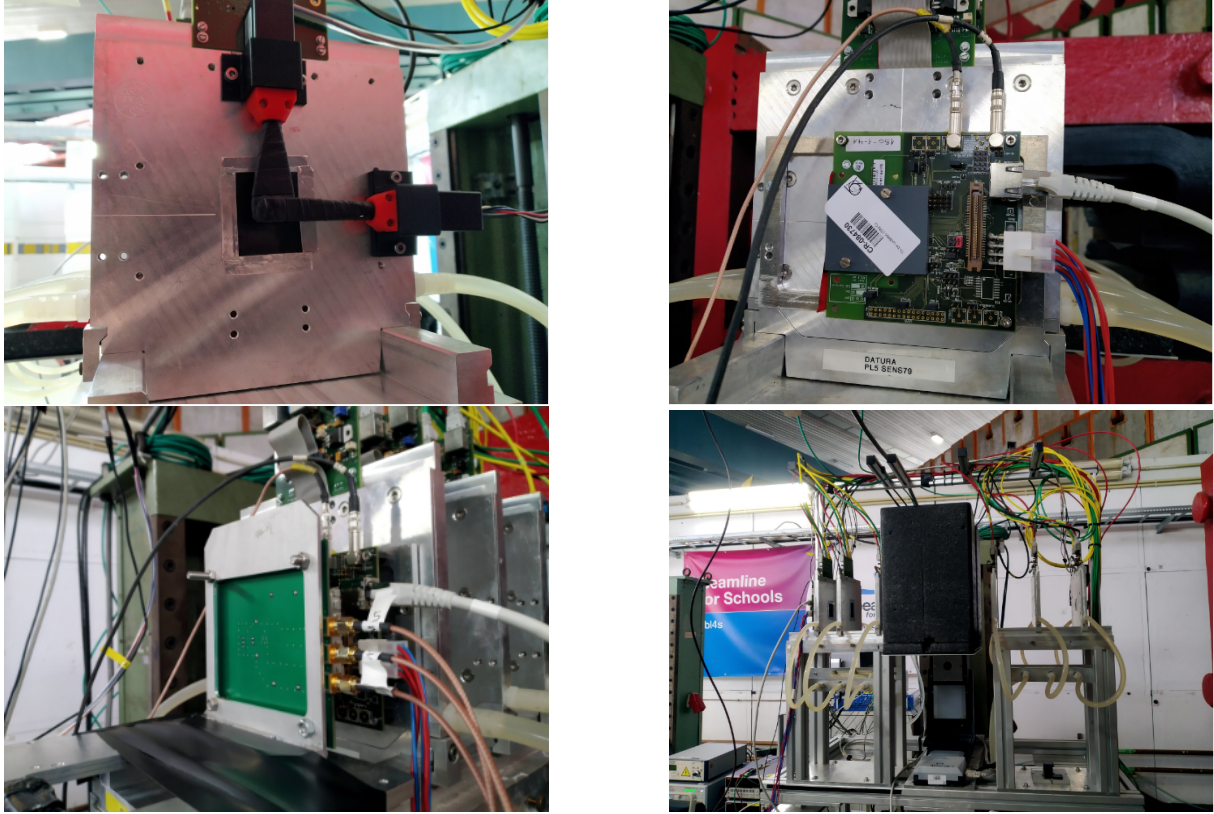


Figure 23: Details from the beam telescope: Scintillators (top left), FE-I4 plane (top right), SiPM (bottom left) and the complete beam telescope with cooling box covering the DUTs (bottom right).

#### 4.1.2 Data acquisition

Two types of data were recorded. The first type contains the particle position information from the telescope and the FE-I4. The second type contains the waveform signals from the DUTs and the SiPM, which was recorded with a four-channel oscilloscope of 10 GS/s and a 2 GHz bandwidth. A region of interest (ROI) was defined on the FE-I4, so only signals within the ROI cause a trigger. The ROI has the size of the SiPM ( $3 \times 3 \text{ mm}^2$ ) and contains the projected areas of the DUTs and SiPM. Optimal alignment is necessary in order to perform time measurements. A Trigger Logic Unit (TLU) combines the triggers from the FE-I4 and the downstream scintillators, if both trigger within a short timeframe, a signal is sent to the oscilloscope to record the waveform. A sufficient time offset is needed to record the signal that arrived previous to the trigger. When the oscilloscope is triggered it sends a TTL pulse back to the TLU module to ensure synchronisation of the oscilloscope with the telescope and FE-I4 plane. Synchronisation is essential for the offline analysis, where tracking data from the

telescope has to be matched to the corresponding waveforms from the DUTs.

#### 4.1.3 Sensors

The sensors that were tested during this testbeam campaign were from Fondazione Bruno Kessler (FBK) in Italy and the Institute of Microelectronics of Chinese Academy of Sciences (IME). The IME sensors were of two different types. One is from the University of Science and Technology of China (USTC), the other one is from the Institute of High Energy Physics (IHEP). In the data the first one will be denoted by USTC and the second one by IMEv2. A list of all the sensors is shown in table 5.

*Table 5: This is a list of the FBK, USTC-IME, and IHEP-IME sensors that were studied during the DESY testbeam campaign in 2022.*

Device name	Vendor	Implant	Irradiation type	Fluence [ $n_{eq}/cm^2$ ]
FBK-W19	FBK	boron + carbon	neutrons	0
FBK-W19 4.0E14	FBK	boron + carbon	neutrons	$4.0 \cdot 10^{14}$
FBK-W19 1.5E15	FBK	boron + carbon	neutrons	$1.5 \cdot 10^{15}$
FBK-W19 2.5E15	FBK	boron + carbon	neutrons	$2.5 \cdot 10^{15}$
USTC-W17 1.5E15	USTC-IME	boron + carbon	neutrons	$1.5 \cdot 10^{15}$
USTC-W17 2.5E15	USTC-IME	boron + carbon	neutrons	$2.5 \cdot 10^{15}$
IMEv2-W7Q2 1.5E15	IHEP-IME	boron + carbon	neutrons	$1.5 \cdot 10^{15}$
IMEv2-W7Q2 2.5E15	IHEP-IME	boron + carbon	neutrons	$2.5 \cdot 10^{15}$

## 4.2 Data-analysis: Charge collection

For the data analysis we will first analyse the charge collection which needs to be above 4 fC. In order to analyse the data it is important to get rid of the noise. This can be done by looking at a couple of factors and make cuts in the data if they fall outside of the requirements. For the charge collection analysis we do not want to make a hard cut in the charge collection, so instead we can look into the pulse height. We will also make use of the tracking data of the telescope which provides us with position and timing information. The position information lets us select data within the region of the sensor. The timing information tells us the time of arrival compared to the other components of the telescope and lets us select a specific time frame.

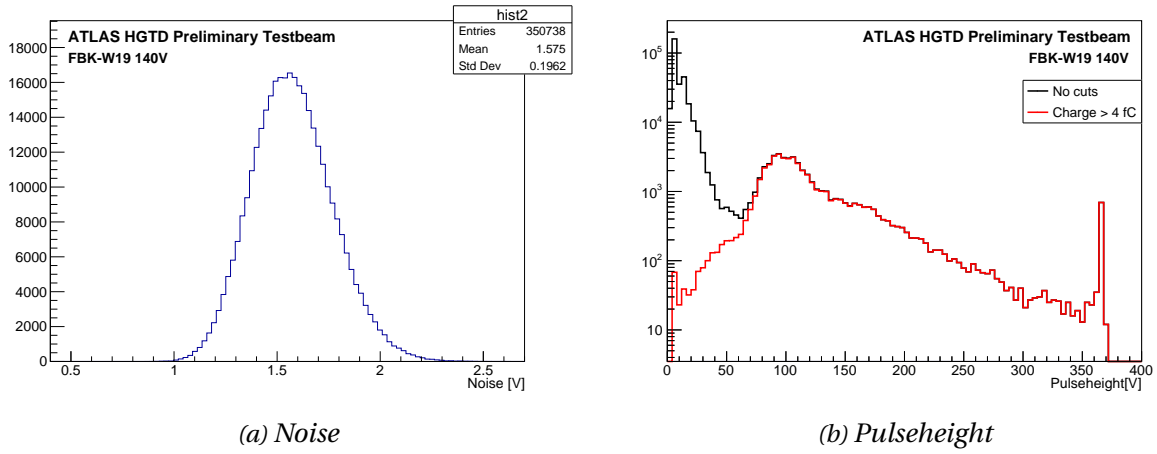


Figure 24: (a) is a histogram of the noise of the unirradiated FBK-W19 sensor. (b) The black line shows the pulse height without any cuts. The red line shows the pulse height with a 4fC charge cut. This shows that the peak on the left consists largely of noise, while the peak on the right shows the actual signal.

#### 4.2.1 Pulse-height cut

For the pulse-height cut we will look at the pulse-height distribution. Signals with lower pulse height are more likely to be noise, so we will only allow events above a certain pulse-height. We will scan for several different pulse-height cuts and analyse the effect on the charge collection and the ratio of negative-charge events. Since the real signal must have a positive charge, the ratio of negative-charge events gives us a measurement for the amount of noise in the data set.

We want to do a scan of 10 different pulse-height cuts and look at the effect on the charge collection and the fraction of events with negative charge collection. The start of the scan will be at three times the mean of the noise (see figure 24a). For the final point of the scan we compare the pulse height without cuts with the pulse height with a 4fC charge cut (see figure 24b). The point where the two histograms come together will be the final point in the scan. In the case of figure 24 the scan will run from 4 to 80.

The result of the pulse-height scan for an unirradiated FBK sensor is shown in figure 25. For the purpose of clarity this graph only shows 5 pulse-height cuts instead of 10. In graph 25a we see that there is a clear distinction between the noise peak on the left and the signal peak on the right. This means that we can choose our pulse-height cut rather high without cutting into the signal peak. In figure 25c we see that around 42V the fraction of negative inputs gets around 5%. Checking with 25b shows us that a pulse-height cut of 42 leaves us with a very small noise peak on the left, while not cutting into the signal peak on the right. We choose the pulse-height cut a bit conservative and will combine it with other cuts to get rid of the small noise peak that is left.

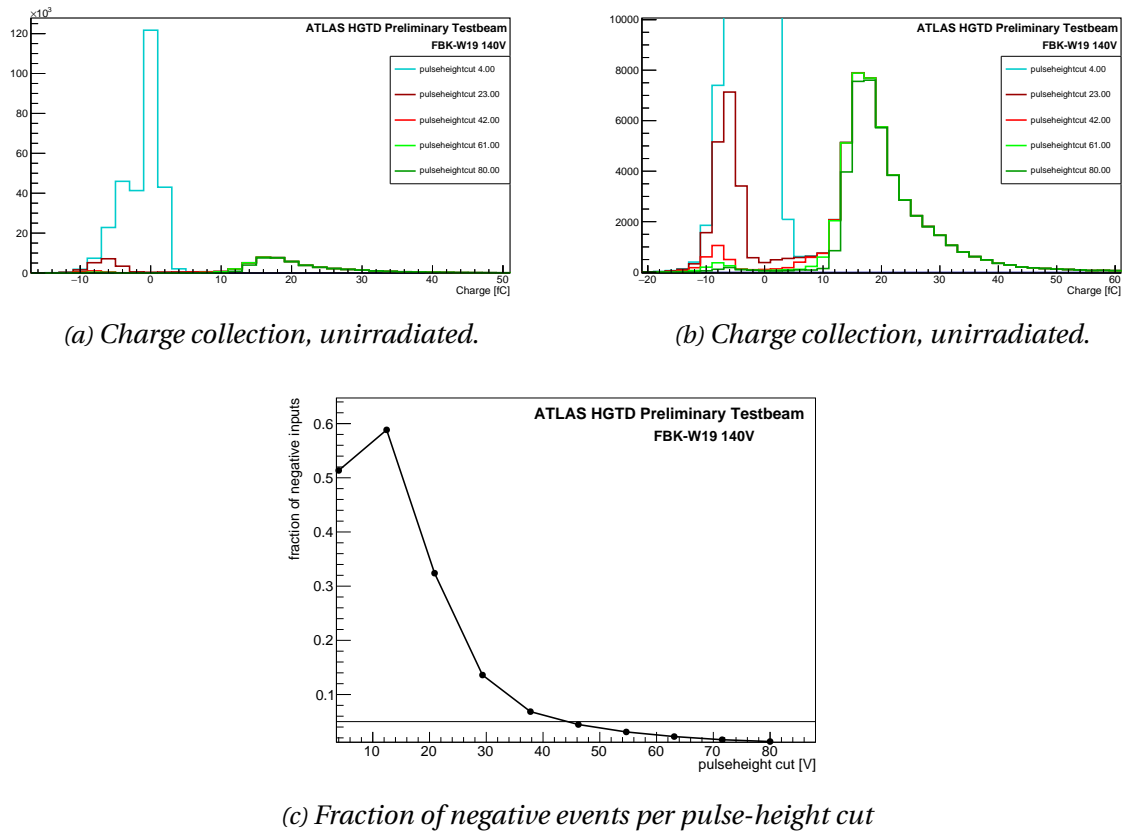
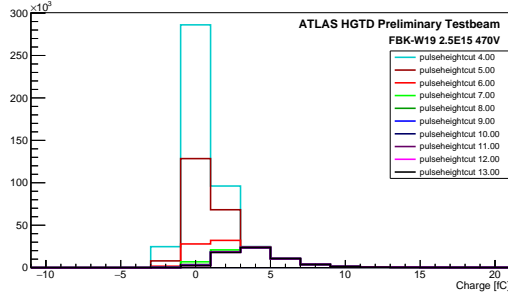
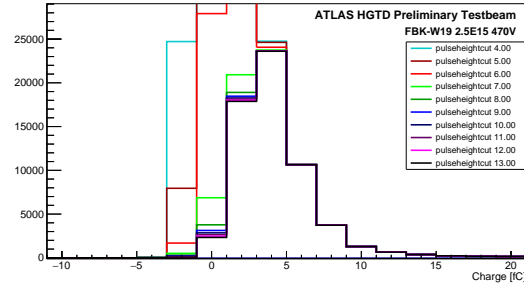


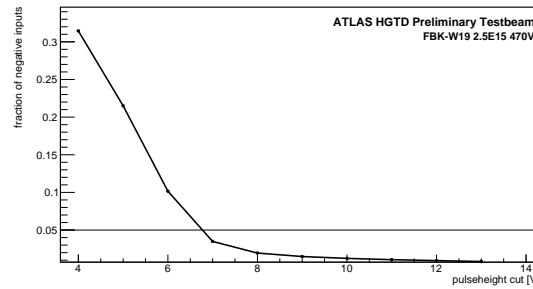
Figure 25: This is the pulse-height scan of the unirradiated sensor FBK-W19 operated at 140V. (a) shows the charge collection histograms for a range of pulse-height cuts. (b) shows a zoomed in version of (a). (c) shows the fraction of events with negative charge collection per pulse-height cut.



(a) Charge collection, irradiated.



(b) Charge collection, irradiated.



(c) Fraction of negative events per pulse-height cut

Figure 26: This is the pulse-height scan of the irradiated sensor FBK-W19 at  $2.5 \cdot 10^{15} n_{eq}$ , operated at 470V. (a) shows the charge collection histograms for a range of pulse-height cuts. (b) shows a zoomed in version of (a). (c) shows the fraction of events with negative charge collection per pulse-height cut.

If we look at the pulse-height scan for an irradiated sensor in figure 26, we see that the noise peak and signal peak are joined together and the charges are much lower. We see that for a pulse-height cut around 7V the fraction of negative events is around 5%. For this pulse-height cut, the green line in figure 29b shows that the big peak around zero vanishes while the signal peak stays in tact.

By looking at multiple DUTs and multiple levels of irradiation it was found that a fraction of 5% negative events resulted in a pulse-height cut that cuts out most of the noise while not cutting into the signal peak.

#### 4.2.2 Geometrical cut

The second cut we will look into is the geometrical cut. In order to do this we look at the reconstructed tracks in the plane of the sensor. To find the location of the sensor we temporarily require that the signal in the chip must be over 4fC, this selects the tracks that created an actual signal in the sensor. Figure 27 shows the track positions with and without the cuts. In figure 27a, without any cuts, we can see the beam profile. In figure 27b, with the 4fC cut, we can see the location of the chip. Now we can select a region of approximately  $1 \times 1$  mm and



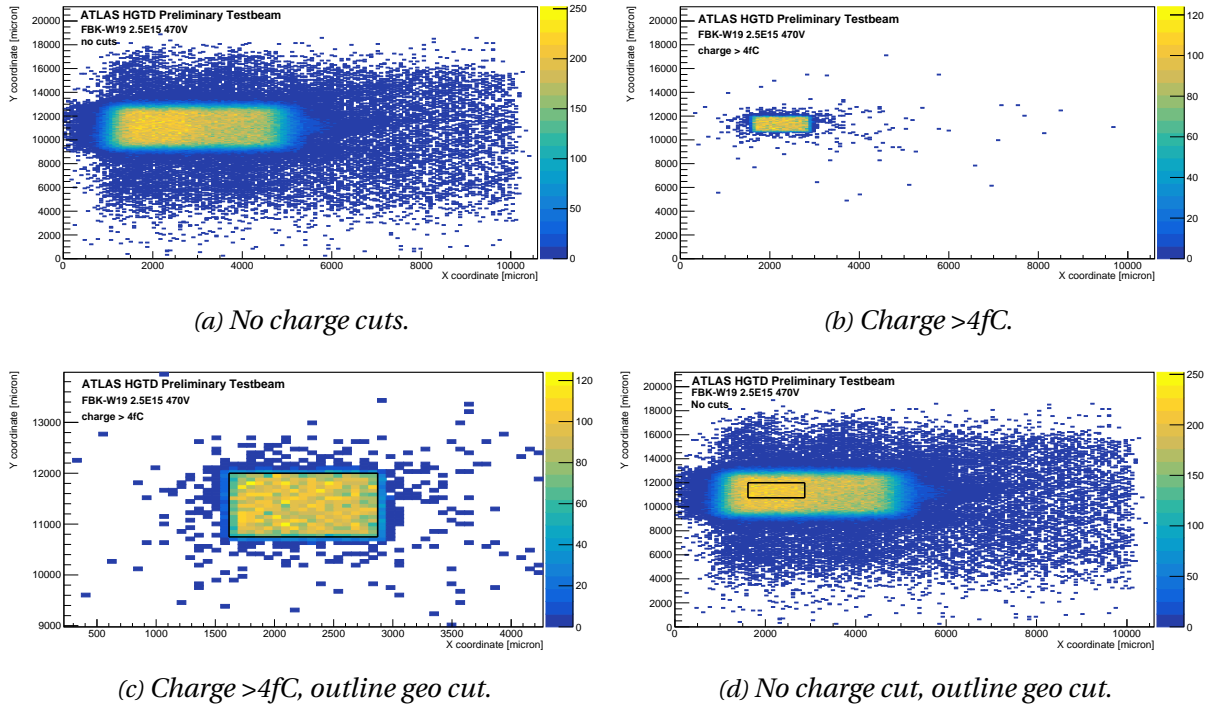


Figure 27: These figures show the track reconstruction in the plane of the FBK-W19 sensor with an irradiation level of  $2.5 \cdot 10^{15} \text{ n}_{\text{eq}}/\text{cm}^2$ . (a) does not apply any cuts, and the figure we see resembles the beam profile. (b) is the result of the 4fC charge cut. The outline of the sensor is clearly visible. (c) shows the selected region for the geometrical cut when the 4fC charge cut is applied. (d) shows the final geometrical cut without any other cuts applied.

this will be the geometrical cut. The exact size of the sensor varies per vendor, so the selected region also varies slightly. In figure 27c we see the selected region for FBK-W19 chip with an irradiation level of  $2.5 \text{ n}_{\text{eq}}/\text{cm}^2$  as an example. In figure 27d we see the selected data without any cuts.

#### 4.2.3 Time cut

The last cut is the time cut. We look at the time difference between the DUT and the SiPM. Since the beam consist of the same particles with the same energy the time difference between the two sensors should be constant. As a measurement for the time of the signal we look at CFD, the constant fraction denominator. This is the time at which the signal crosses a certain fraction (20% for CFD20, 50% for CFD50) of its total height. For the SiPM reference we use CFD50 while for the DUTs we use CFD20 [8]. Finally a section of 1000 ps is selected around the peak.

A time cut for one of the FBK-W19 with an irradiation level of  $2.5 \cdot 10^{15} \text{ n}_{\text{eq}}/\text{cm}^2$  is shown in



figure 28. There are two peaks visible here, one around 1000 ps and one around 0 ps. The big peak around 1000 is the peak that contains the actual signal. The peak around 0 contains noise and is caused by other non-bonded pixels of the chip. These extra peaks are also seen in some other sensors and will be discussed at the end of this chapter.

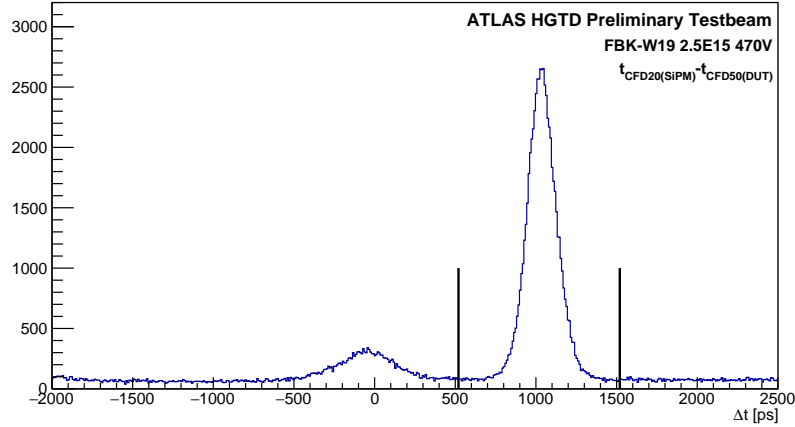
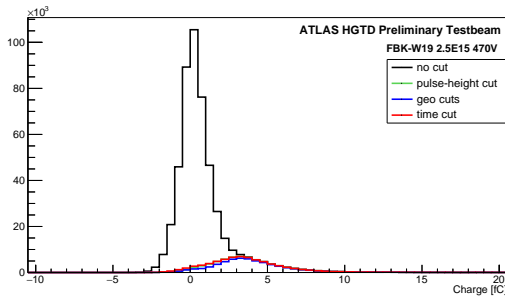


Figure 28: This figure shows the time difference between CFD20(SiPM) and CFD50(DUT). The DUT here is the FBK-W19 with an irradiation level of  $2.5 \cdot 10^{15} n_{eq}/cm^2$ .

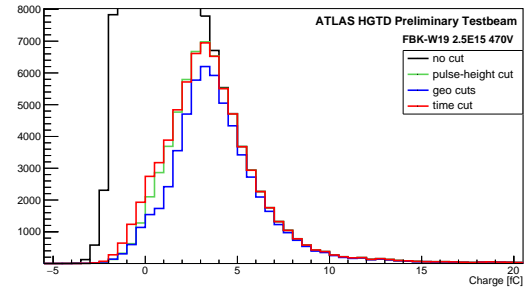
#### 4.2.4 The effect of the cuts

After defining the three different types of cuts we had a look at how they affect the charge collection when they are applied individually or combined. The results are displayed in figure 29. Figure 29a and 29b show the charge graphs without cuts and with single cuts. We see that the charges for the pulse-height cut and time cut are almost the same, while the charge for the geometrical cut has a slightly lower peak. But more interesting is figure 29c, here we see that the combination of pulse-height cut and time cut is significantly higher than the others, and the other three combinations with the geometrical cut are almost the same.

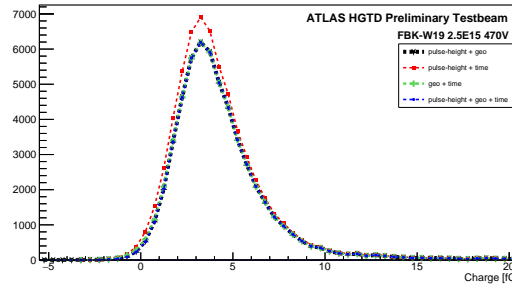
Since the geometrical cut made such a big difference it was important to know where this difference was coming from. Therefore we looked at the geometrical plot and applied the pulse-height cut as shown in figure 30. The black rectangle around the yellow spot is the sensor. We are interested in the events that do pass the pulse-height cut but do not pass the geometrical cut, so this is all the events outside of black rectangle. We see that the geometrical cut is placed correctly since the bright yellow spot (that indicates the sensor) is located inside the rectangle, but we also see that outside of the rectangle there are still a lot of events. From this we can conclude that the geometrical cut is absolutely necessary.



(a) Charge collection, comparing cuts.



(b) Charge collection, comparing cuts.



(c) Charge collection. Comparing combinations of cuts.

Figure 29: This is the pulse-height scan of the irradiated sensor FBK-W19 at  $2.5 \cdot 10^{15} n_{eq}/cm^2$ , operated at 470V. (a) shows the charge collection histograms for a range of pulse-height cuts. (b) shows a zoomed in version of (a). (c) shows the fraction of events with negative charge collection per pulse-height cut.

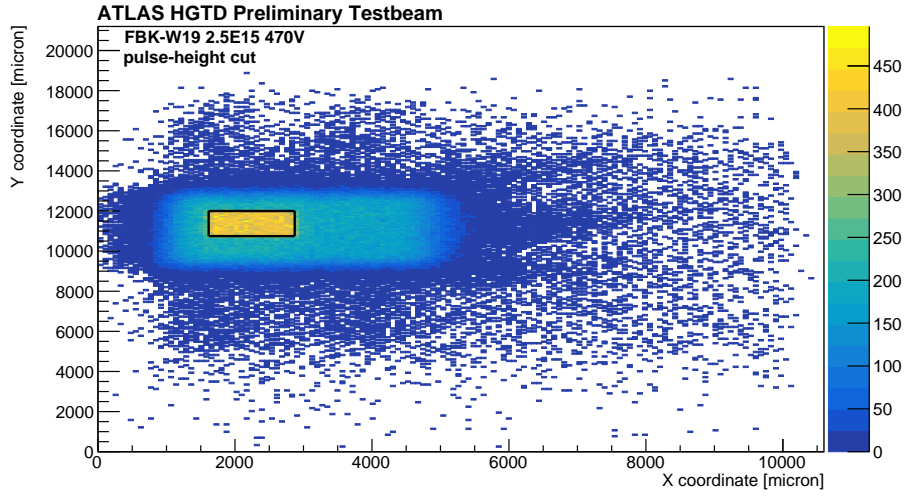


Figure 30: This is a geometrical plot where only the pulse-height cut is applied. This is for the FBK-W19 sensor with a fluence of  $2.5 \cdot 10^{-15} n_{eq}/cm^2$  at 470V bias voltage. The sensor itself is indicated with the black rectangle.

We also applied a Langaus fit to the different combinations of cut. A Langaus fit is a convolution of a Landau and Gaussian fit and the value we are most interested in is the most probable value (MPV). The MPVs for the different cuts can be found in table 6. For the single cuts we see that there is quite some variation between the MPVs where the geometrical cut clearly gives the highest MPV. For the combined cuts we see that the values get much more stable, but we still see a jump of about 0.1 fC when the geometrical cut is added.

Table 6: This table shows the MPV (most probable value) for the charge collection for different cuts and combinations of cuts. These values are from the FBK-W19 at  $2.5 \cdot 10^{15} n_{eq} cm^{-2}$ , operated at 470V. Ph means pulse-height cut, Geo is the geometrical cut and Time is the time cut.

Cut	MPV [fC]
Ph	2.719
Geo	2.936
Time	2.686
Ph + Geo	3.073
Ph + Time	2.979
Geo + Time	3.066
Ph + Geo + Time	3.070

The other sensors showed a similar situation as the sensor discussed above. The geometrical cut lowered the charge peak but the other cuts gave an almost similar charge plot. Finally we

chose to apply all three cuts to all of the data.

#### 4.2.5 Results

After applying the pulse-height, geometrical, and timing cut, the MPV for each graph was found using a langaus fit as can be seen in figure 31. In this picture the MPV is given as ml, sg and sl are the sigmas for the Gaussian en Landau function.

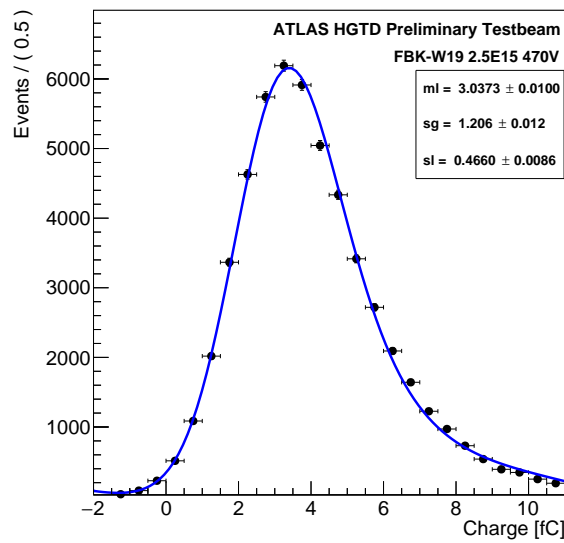


Figure 31: This shows the charge for the FBK-W19 sensor with a fluence of  $2.5 \cdot 10^{15} n_{eq}/cm^2$  at 470V bias voltage. The fit is a Langaus fit.

The results for the FBK-W19 chip with different fluences are shown in figure 32. This figure clearly shows that for higher fluences it is necessary to further increase the bias voltage. But for all fluences it is possible to reach the 4fC charge line.

The charge collection results for the other chips are shown in figure 33. Figure 33a shows the results for the chips with a fluence of  $1.5 \cdot 10^{15} n_{eq}/cm^2$ . It shows that all three chips can reach a charge collection higher than 4 fC. Figure 33b shows only two chips with a fluence of  $2.5 \cdot 10^{15} n_{eq}/cm^2$  since the IMEv2 chip of this fluence was not-responding. Both chips can reach the 4 fC charge collection if the bias voltage is large enough. All these results are comparable to the results from the 2023 test-beam paper [9].

It is interesting to see that the result from this work are the same as the results the 2023 test-beam paper since there were some differences in the data selection. First, the 2023 paper did not take a pulseheight cut for the DUTs, instead they took a pulse-height cut for the SiPM of

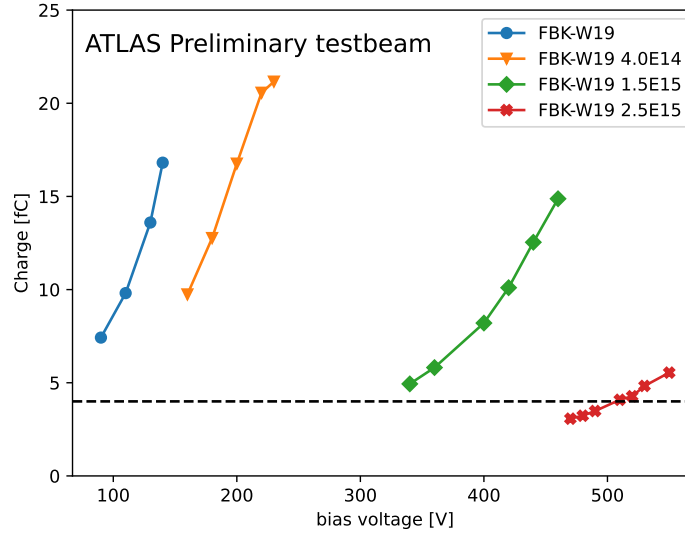


Figure 32: Charge for the FBK-W19 chip for different fluences.

three times the noise level. Second, for the geometrical cut they took only the inner region of  $0.5 \times 0.5 \text{ mm}^2$  while this work took the geometry of the entire chip. Finally, for the timing cut they took a 2 ns window while this work only took a 1 ns window. Overall the data looks very much the same, so it seems that both methods work.

### 4.3 Data analysis: Time Resolution

The time resolution is one of the most important values for the LGAD and should be below 70 ps at the end of its lifetime. This value can be calculated by measuring the distribution of the time of arrival (TOA) differences between the DUTs and the SiPM. Since the TOA of the DUTs and the SiPM can be considered independent the time resolutions can be calculated with the following formulas:

$$\sigma_{\text{DUT1}} = \sqrt{\frac{\sigma_{12}^2 + \sigma_{13}^2 - \sigma_{23}^2}{2}} \quad (7)$$

$$\sigma_{\text{DUT2}} = \sqrt{\frac{\sigma_{12}^2 + \sigma_{23}^2 - \sigma_{13}^2}{2}} \quad (8)$$

Here  $\sigma_{\text{DUT1/DUT2}}$  is the timing resolution of respectively DUT1 and DUT2.  $\sigma_{12}$  is the distribution of the TOA difference between DUT1 and DUT2,  $\sigma_{13}$  is determined by DUT1 and the

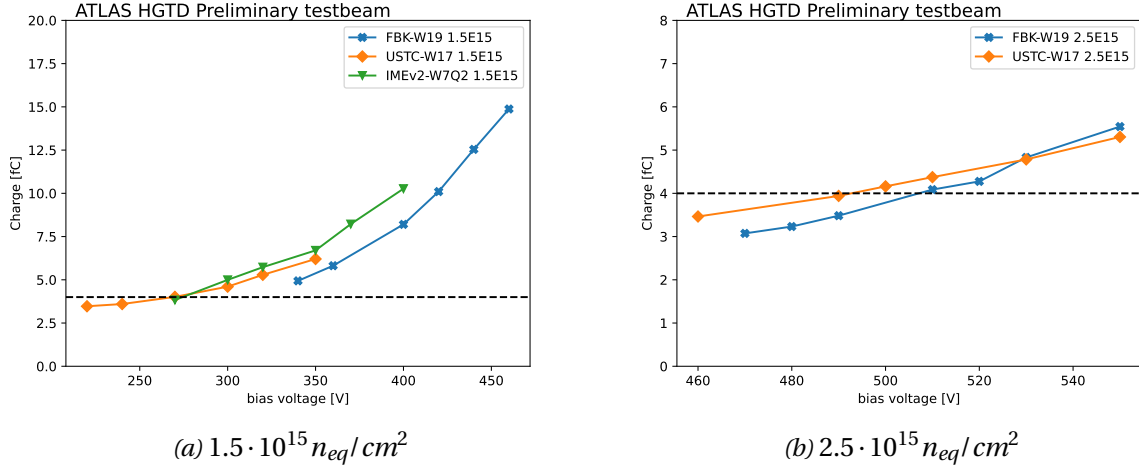


Figure 33: These are the charge collection results. (a) shows the results for chips with a fluence of  $1.5 \cdot 10^{15} n_{eq}/cm^2$ , (b) shows the results for chips with a fluence of  $2.5 \cdot 10^{15} n_{eq}/cm^2$

SiPM, and  $\sigma_{23}$  is determined by DUT2 and the SiPM.

Just as with the charge collection analysis some data selection was done to get rid of the noise and a fit was applied. For the DUTs the same data selection was used as for the charge collection analysis. We also applied an extra pulse-height cut of three times the noise to the SiPM to further clean up the TOA difference plots. Since the TOA differences are normally distributed they could be fitted with a Gaussian fit as displayed in figure 34. The standard deviations, sigma, of these fits give our values for  $\sigma_{12}$ ,  $\sigma_{13}$ , and  $\sigma_{23}$ . So in our example of figure 34 this means  $\sigma_{12} = 70.66 \pm 1.90$  ps,  $\sigma_{13} = 90.69 \pm 2.27$  ps, and  $\sigma_{23} = 78.93 \pm 2.23$  ps. This gives  $\sigma_{DUT1} = 55.80 \pm 2.75$  ps for the IMEv2 sensor and  $\sigma_{DUT2} = 41.30 \pm 3.72$  ps for the USTC sensor.

#### 4.3.1 Results

The results for the FBK, USTC, and IMEv2 sensors at a fluence of  $1.5 \cdot 10^{15} n_{eq}/cm^2$  are shown in figure 34. They are all under the required resolution 70ps. Compared to the results from the 2023 testbeam paper [9] there are some small differences. This might be due to a difference in data selection or it is influenced by the choice in fit region. Another thing that we can notice are the relatively large error bars for the FBK sensor. This was likely caused by the reference DUT (the FBK-W10) being very noisy.

#### 4.4 Extra time peaks

When looking into the TOA differences without any cuts we came across some unexpected peaks in the unirradiated FBK-W19 sensor. Upon further analysis these peaks were also

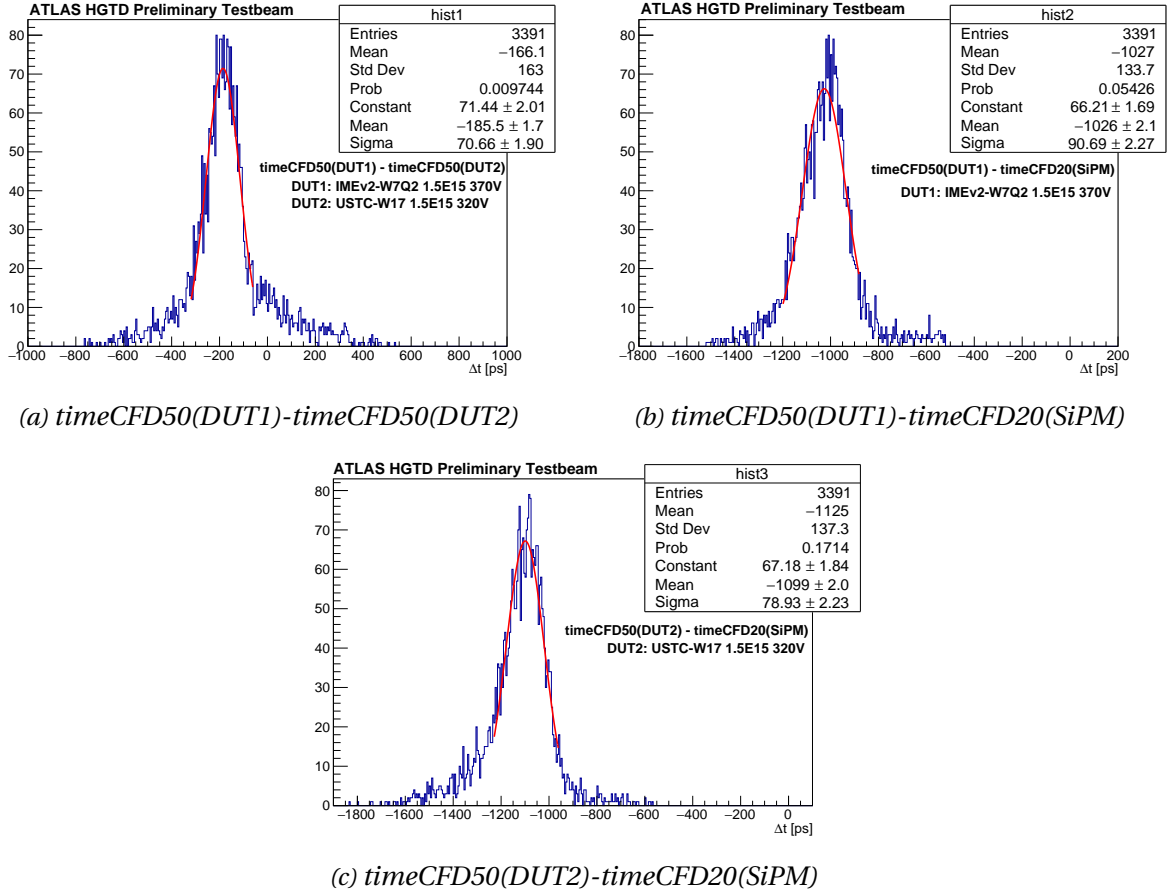


Figure 34: These graphs show the Gaussian fits for the time-of-arrival differences for the time resolution analysis. These graphs are for the IMEv2-W7Q2 at 370V bias voltage and USTC-W17 at 320V bias voltage, both at a fluence of  $1.5 \cdot 10^{15} n_{eq}/cm^2$ . (a) shows the difference in time of arrival between DUT1 and DUT2 with  $\sigma_{12} = 70.66 \pm 1.90ps$ , (b) shows the difference between DUT1 and the SiPM with  $\sigma_{13} = 90.69 \pm 2.27ps$ , (c) shows the difference between DUT2 and the SiPM with  $\sigma_{23} = 78.93 \pm 2.23ps$ .

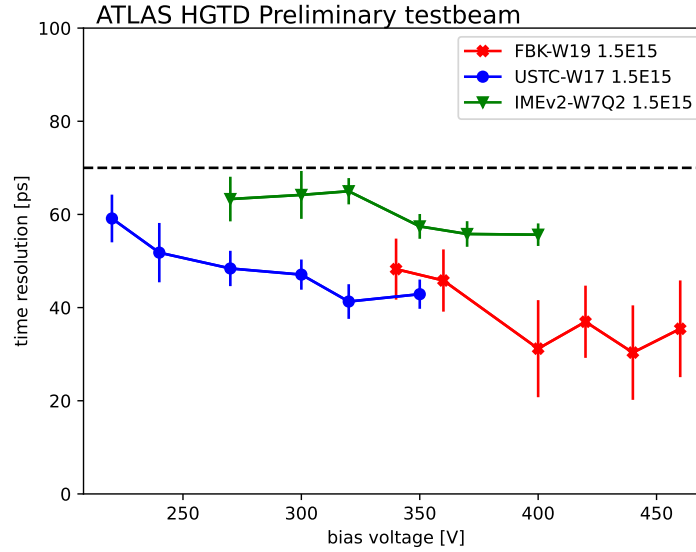


Figure 35: These are the time resolution results for the chips with a fluence of  $1.5 \cdot 10^{15} n_{eq}/cm^2$ .

found in the FBK-W19 sensor with a fluence of  $2.5 \cdot 10^{-15} n_{eq}/cm^2$ . Both these sensors are  $2 \times 2$  samples with one active pad and the other pads connected to ground. An example of the time peaks for the unirradiated sensor is shown in figure 36. This figure shows the difference in TOA between the SiPM and the unirradiated FBK-W19 sensor at 140V bias voltage. Instead of a single peak this contained 2 other peaks, of which the second peak is much larger than the first peak.

The behaviour of the individual peaks was further analysed by looking at their individual geography and charge plots as shown in figure 37. These plots were produced by placing a timing cut around the peaks as shown by the lines in figure 36. For peak 1 the charge could be fitted with a Languas fit with  $MPV \approx 16.65$  fC, indicating that the first peak contains the actual signal. For peak 2 and 3 the charge was fitted with a Gaussian fit with a mean of respectively  $-3.98$  fC and  $0.24$  fC. They both look like noise although it is remarkable to see that the mean of peak 2 is around  $-4$  fC instead of around  $0$  fC as is expected with noise. If we look at the geography plots we immediately notice that this is a  $2 \times 2$  sensor. Peak 1 is clearly coming from the active pad, while the events from peak 2 and 3 are mostly coming from the inactive pads. Since the inactive pads were grounded they were not expected to induce a signal, so this is worth looking further into.

The time plot for the other  $2 \times 2$  sample, the FBK-W19 sensor with a fluence of  $2.5 \cdot 10^{15} n_{eq}/cm^2$ , is shown in figure 38. This plot also shows an extra time plot, although it is only one extra peak instead of two, and the second peak is much lower.

Just like for the unirradiated sensor we had a look at the charge and geometrical plots for the



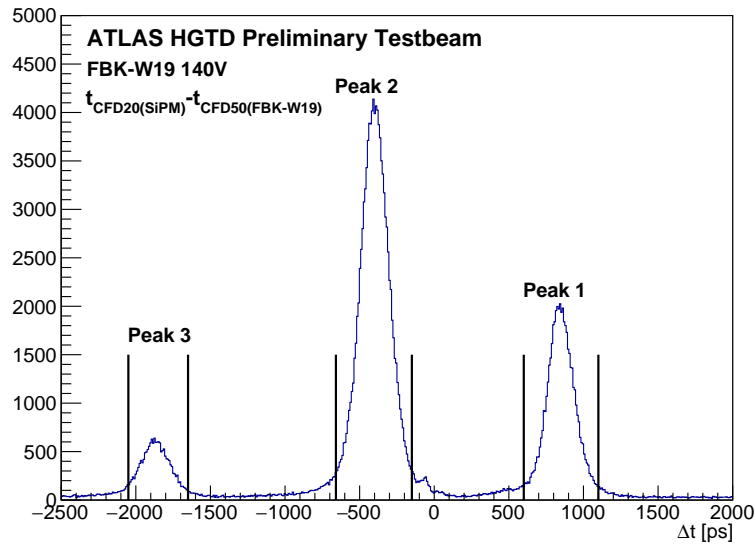
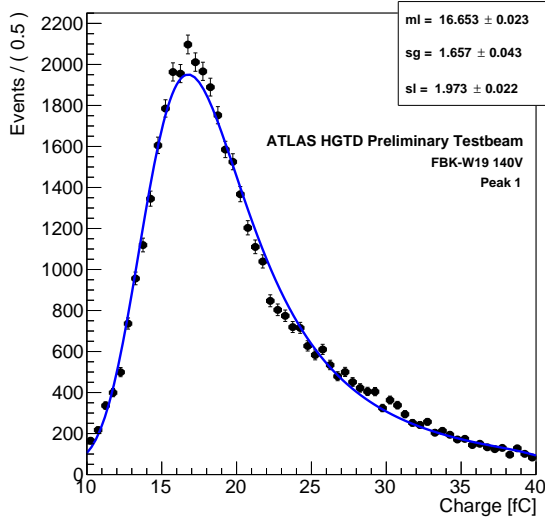


Figure 36: This figure shows the time difference between the SiPM and the FBK-W19 sensor at 140V. It shows three peaks instead of the expected one peak.

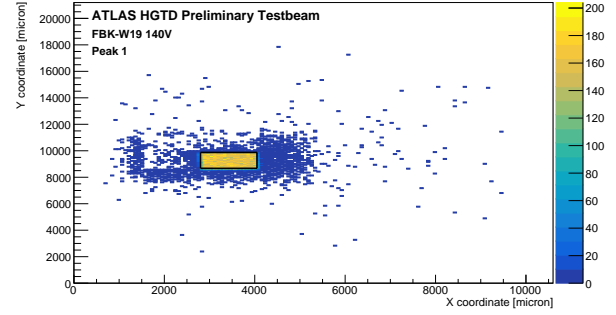
individual time peaks of the irradiated sensor. These results are shown in figure 39. For the first peak the charge plot is fitted with a Langaus and  $MPV = 5.31fC$ . The geometrical plot for this peak also shows the signal coming from the active sensor. For the second peak we could fit a Gaussian over the charge plot with a mean of  $0.16fC$  as we expect of noise. The geometrical plot shows that the signal originates from outside the active pad, which is indicated by the black rectangle. This geometrical picture is different in the sense that not all 3 active pads light up like in the unirradiated sensor. It is possible that this sensor has another issue compared to the irradiated one.

For further analysis we had a look into the waveforms. The waveforms for the unirradiated sensor are in figure 40. The waveforms for peak 1 typically looked like figure 40a, this pulse looks like it is induced by an actual particle. The waveforms for peak 2 and 3 typically looked like figure 40b and 40c. This does not look like a signal peak but more like ringing from electronics. Possibilities are a problem with the wirebonding or mounting. For further analysis this the sensor could be tested with transient current technique (TCT) where a pulse gets injected into a certain part of the sensor.

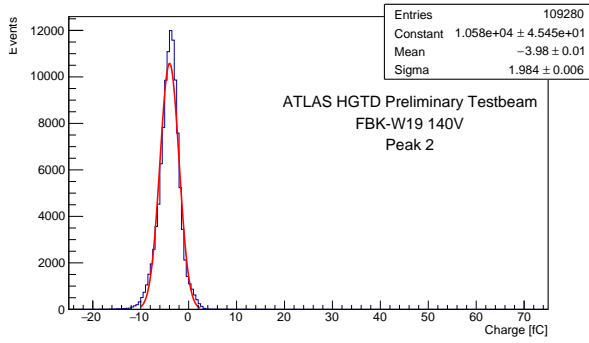
The waveforms from the irradiated FBK-W19 sample are shown in figure 41. For this sensor the pulses from the extra time peak typically looked like 41b, which looks exactly the same as the pulse coming from the active pad. So the extra time peak seems to have another origin than the timepeaks of the unirradiated sensor. For the irradiated sensor the next step would be to average the waveforms and see if the waveform changes with bias voltage. If it does that indicates that it has to do with particles, otherwise it is something else.



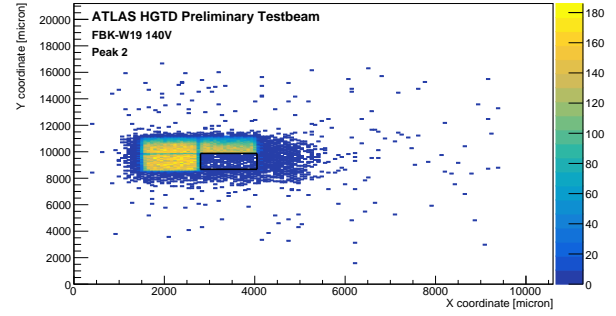
(a) Peak 1, charge



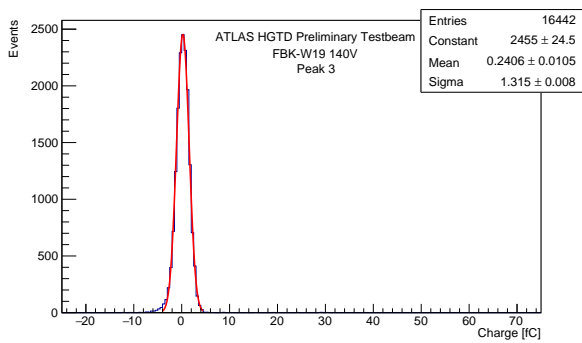
(b) Peak 1, geo



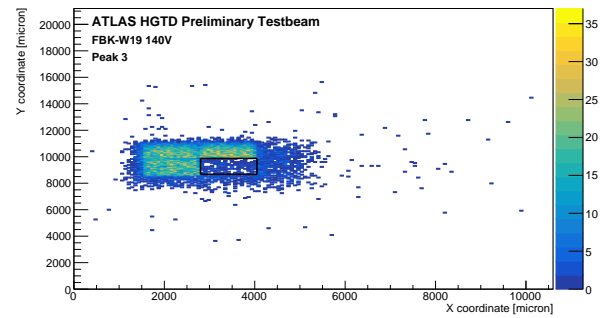
(c) Peak 2, charge



(d) Peak 2, geo



(e) Peak 3, charge



(f) Peak 3, geo

Figure 37: These are the charge and geometrical plots for each of the peaks as seen in figure 36. They are of the unirradiated FBK-W19 sensor which is a  $2 \times 2$  sensor with one pad connected and the other pads connected to ground. (a) is the charge plot for the first peak. It is fitted with a Langaus with  $MPV = 16.53fC$ . (b) is the geometrical plot for the first peak. Only one pad lights up indicating that all the signal indicates from the active pad. (c) is the charge plot for the second peak, fitted with a Gaussian and a mean of  $-3.96fC$ . (d) is the geometrical plot for the second peak. The black rectangle indicates the position of the active pads, and it is clear that the second peak originates from the three inactive pads. (e) is the charge plot for the third peak, it is fitted with a Gaussian and the mean is  $0.24fC$ . (f) is the geometrical plot for the third peak. The third peak also seems to be induced by the inactive pads.

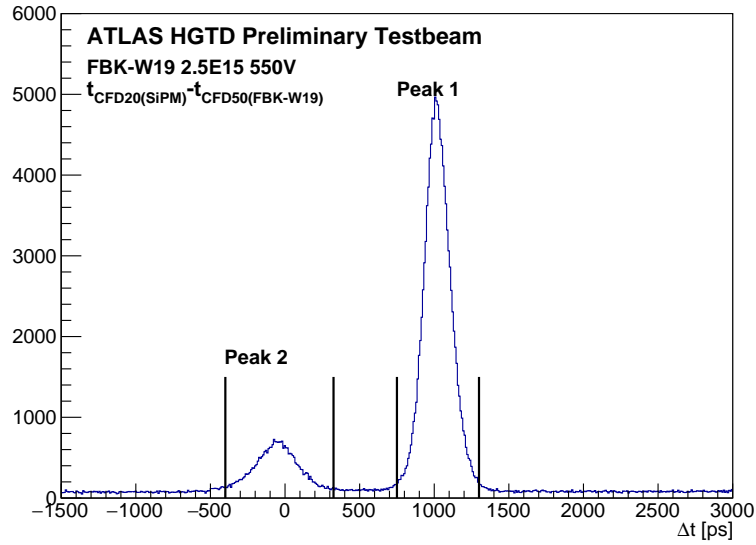


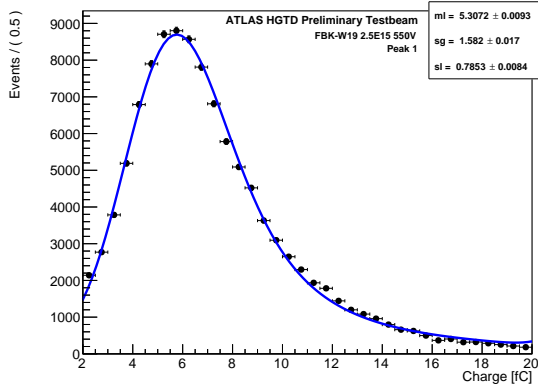
Figure 38: This figure shows the time difference between the SiPM and the FBK-W19 sensor with a fluence of  $2.5 \cdot 10^{15} n_{eq} cm^{-2}$  at 550V. It shows two peaks instead of the expected one peak.

## 5 Conclusion

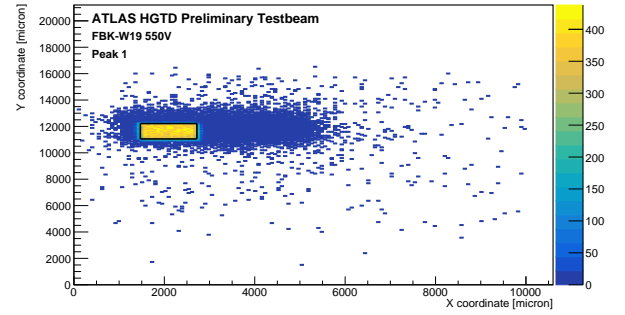
### 5.1 IV/CV

The IV and CV measurements were done for the unirradiated HPK-P2 sensors with different boron doses. For the IV and CV measurements the results were as expected. The  $I_{leak}$  were all under 1nA, which is way below the maximum 5 $\mu$ A.  $V_{gl}$  was in the expected range of 50.5 – 54.5V and the  $V_{vd}$  was typically 5 – 6V on top of the  $V_{gl}$ .

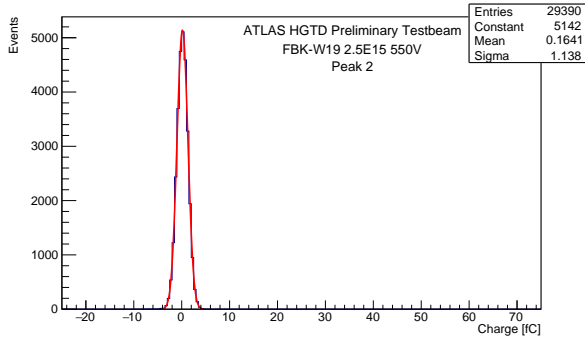
Despite this both the IV measurements as the CV measurements could be improved in the future. The IV measurements can be improved by taking the mean or the median out of several measurements. An SMU with a range below 1.00000  $\mu$ A could possibly help as well. For the CV measurement the most important improvement would be to calibrate the system for the cable length, especially when using the 1MHz AC frequency. There also should be further research in the accuracy of the 1MHz measurements since the dissipation factor was quite high, especially for low bias voltages. It could be that the calibration for cable length already fixes the problem with the high dissipation factor, but it would also be good to see the result for the series model instead of the parallel model. Despite the difficulty with the high dissipation factor, the change in frequency barely changed the  $V_{vd}$  and  $V_{gl}$ , so the 1MHz measurements were used for all the results.



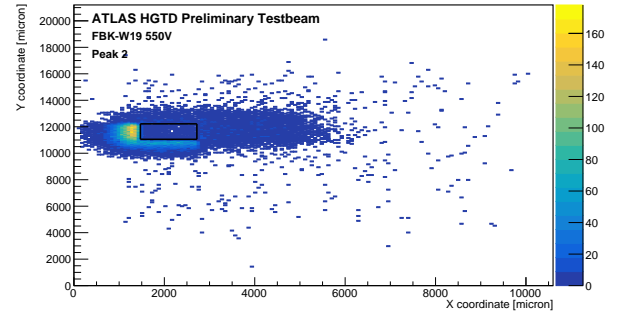
(a) Peak 1, charge



(b) Peak 1, geo

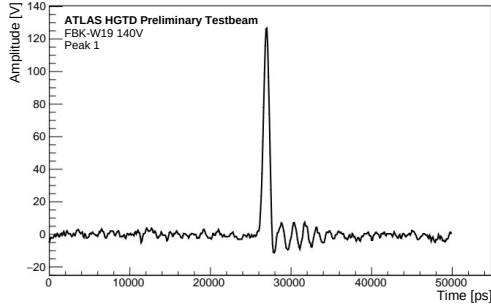


(c) Peak 2, charge

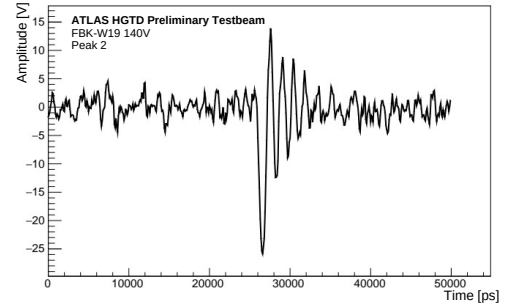


(d) Peak 2, geo

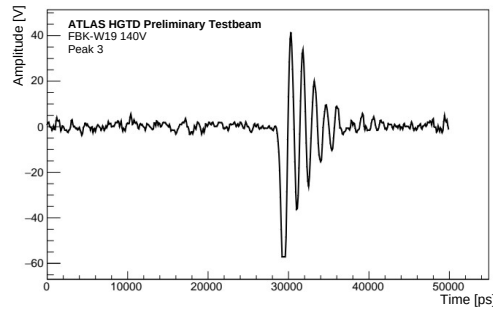
Figure 39: This figure shows the charge and geometrical plots from the two peaks in figure 38. They are from the FBK-W19 with a fluence of  $2.5 \cdot 10^{15} n_{eq}cm^{-2}$  operated at 550V bias voltage. It is a  $2 \times 2$  sensor with one pad connected and the other three pads connected to ground. (a) shows the charge plot of the first peak with a Langaus fit with MPV = 5.31fC. (b) is the geometrical plot and shows the peak originates from the active pad. (c) is the charge plot of the second peak fitted with a Gaussian and a mean of 0.16fC. (d) is the geometrical plot for the second peak. It shows the signal is coming from outside the active pad (indicated with the black rectangle).



(a) Unirradiated FBK-W19, peak 1

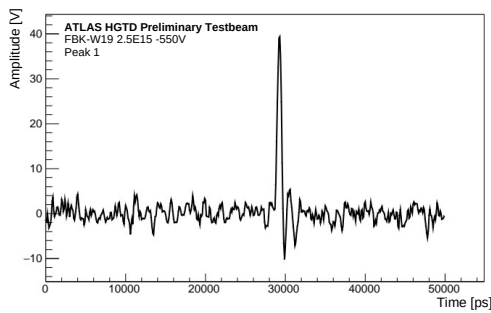


(b) Unirradiated FBK-W19, peak 2

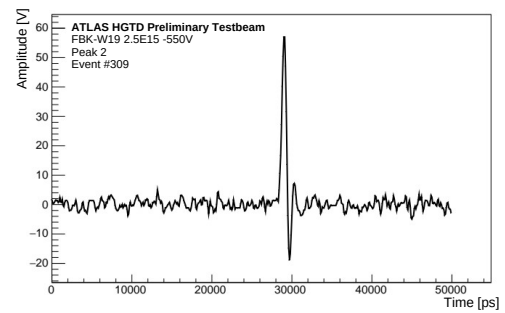


(c) Unirradiated FBK-W19, peak 3

Figure 40: These are waveforms corresponding to the three different time peaks for the unirradiated FBK-W19 sample at a 140V bias voltage. (a) is from peak 1, (b) is from peak 2, and (c) is from peak 3.



(a) FBK-W19 2.5E15 -550V, peak 1



(b) FBK-W19 2.5E15 -550V, peak 2

Figure 41: These are waveforms corresponding to the two different time peaks for the irradiated FBK-W19 sample at a -550V bias voltage. (a) is from peak 1 and (b) is from peak 2.

## 5.2 Testbeam

Three different sensors with different fluences were tested during the testbeam campaign at DESY in 2022. These were the FBK, USTC-IME and IHEP-IME sensors. For all these sensors we determined the charge collection and timing resolution. The results showed that for all sensors with a fluence up to  $2.5 \cdot 10^{15} \text{ n}_{\text{eq}}/\text{cm}^2$  a charge collection of 4fC could be reached. The required time resolution of 70ps could also be reached.

The results from this work were compared to the results from the 2023 testbeam paper [9]. For the data selection the 2023 testbeam paper used a 2ns timing cut, an amplitude cut on the SiPM of three times the noise, and a 2fC charge cut. This work used a pulse-height cut that leaves a fraction of 5% negative events, a geometrical cut around the entire sensor, and a 1 ns timing cut. Despite these differences the results were almost the same.

During the analysis for the timing cut we came across some extra peak for the  $2 \times 2$  FBK sensors. For these sensors only one pad was connected to the readout electronics while the other pads were connected to ground. While the extra time peaks created no problems for the charge and time resolution analysis, it is important to understand the origin of the peaks since they can cause issues later on. Upon further analysis of the time peaks we found out that the first peak was coming from the active pad, while extra time peaks were induced by the inactive pads. Furthermore, the timepeaks from the unirradiated sensor appeared to be caused by ringing of the electronics. It is advised to test the sensor with TCT to find the exact cause of the problem. The extra timepeaks of the irradiated sensor seemed to have a different cause since their waveforms look much like the waveforms from the signal peak. The next step for this sensor would be to look at the average waveforms for the peak and see if they change with bias voltage. If they do change with bias voltage that indicates that the problem has to do with particles, otherwise not.

## References

- [1] Marco Ferrero, Roberta Arcidiacono, Marco Mandurrino, Valentina Sola, and Nicolò Cartiglia. *An Introduction to Ultra-Fast Silicon Detectors: Design, Tests, and Performances*. June 2021.
- [2] Simon Hall. *Particle Detectors: Fundamentals and Applications*, volume 118. Oxford University Press, Oxford, England, UK, April 2013.
- [3] Technical Design Report: A High-Granularity Timing Detector for the ATLAS Phase-II Upgrade, June 2020.
- [4] Inc. Keithley Instruments. C-v testing for semiconductor components and devices - applications guide. <https://www.tek.com/en/documents/application-note/c-v-testing-semiconductor-components-and-devices-applications-guide>, 2014.
- [5] The DESY II test beam facility. *Nucl. Instrum. Methods Phys. Res., Sect. A*, 922:265–286, April 2019.
- [6] H. Jansen, S. Spannagel, J. Behr, A. Bulgheroni, G. Claus, E. Corrin, D. G. Cussans, J. Dreyling-Eschweiler, D. Eckstein, T. Eichhorn, M. Goffe, I. M. Gregor, D. Haas, C. Muhl, H. Perrey, R. Peschke, P. Roloff, I. Rubinskiy, and M. Winter. Performance of the EUDET-type beam telescopes. *arXiv*, March 2016.
- [7] C. Agapopoulou, S. Alderweireldt, S. Ali, M. K. Ayoub, D. Bencheikroun, L. Castillo García, Y. H. Chan, H. El Jarrari, A. Falou, A. Ferreira, E. L. Gkougkousis, C. Grieco, S. Grinstein, J. Große-Knetter, J. Guimarães da Costa, S. Guindon, A. M. Henriques Correia, S. Hidalgo, A. Howard, P. J. Hsu, Y. C. Huang, Y. Khoulaki, G. Kramberger, E. S. Kuwertz, J. Lange, C. Li, Q. Li, H. C. Lin, Y. J. Lu, N. Makovec, L. Masetti, R. Mazini, S. M. Mazza, I. Nikolic, G. Pellegrini, A. Quadt, B. Reynolds, C. Rizzi, M. Robles Manzano, A. Rummler, S. Sacerdoti, L. Serin, J. Soengen, Y. Tayalati, S. Terzo, E. Tolley, S. Trincaz-Duvoid, S. M. Wang, and X. Yang. Performance in beam tests of irradiated Low Gain Avalanche Detectors for the ATLAS High Granularity Timing Detector. *J. Instrum.*, 17(09):P09026, September 2022.
- [8] C. Agapopoulou, S. Alderweireldt, S. Ali, M. K. Ayoub, D. Bencheikroun, L. Castillo García, Y. H. Chan, H. El Jarrari, A. Falou, A. Ferreira, E. L. Gkougkousis, C. Grieco, S. Grinstein, J. Große-Knetter, J. Guimarães da Costa, S. Guindon, A. M. Henriques Correia, S. Hidalgo, A. Howard, P. J. Hsu, Y. C. Huang, Y. Khoulaki, G. Kramberger, E. S. Kuwertz, J. Lange, C. Li, Q. Li, H. C. Lin, Y. J. Lu, N. Makovec, L. Masetti, R. Mazini, S. M. Mazza, I. Nikolic, G. Pellegrini, A. Quadt, B. Reynolds, C. Rizzi, M. Robles Manzano, A. Rummler, S. Sacerdoti, L. Serin, J. Soengen, Y. Tayalati, S. Terzo, E. Tolley, S. Trincaz-Duvoid, S. M. Wang, and X. Yang. Performance in beam tests of irradiated Low Gain Avalanche Detectors for the ATLAS High Granularity Timing Detector. *J. Instrum.*, 17(09):P09026, September 2022.

- [9] S. Ali, H. Arnold, S. L. Auwens, L. A. Beresford, D. E. Boumediene, A. M. Burger, L. Cadamuro, L. Castillo García, L. D. Corpe, M. J. Da Cunha Sargedas de Sousa, D. Dannheim, V. Dao, A. Gabrielli, Y. El Ghazali, H. El Jarrari, V. Gautam, S. Grinstein, J. Guimarães da Costa, S. Guindon, X. Jia, G. Kramberger, Y. Liu, K. Ma, N. Makovec, S. Manzoni, I. Nikolic, O. Perrin, V. Raskina, M. Robles Manzano, A. Rummler, Y. Tayalati, S. Trincaz-Duvoid, A. Visibile, S. Xin, L. Xu, X. Yang, and X. Zheng. Performance in beam tests of carbon-enriched irradiated Low Gain Avalanche Detectors for the ATLAS High Granularity Timing Detector. *J. Instrum.*, 18(05):P05005, May 2023.